Journal of Medicinal Chemistry

Article

Cite This: J. Med. Chem. 2018, 61, 2895−2909

pubs.acs.org/jmc

Structure−Activity Relationship in Monosaccharide-Based Toll-Like Receptor 4 (TLR4) Antagonists

Fabio A. Facchini,[†] Lenny Zaffaroni,[†] Alberto Minotti,[†] Silvia Rapisarda,[†] Valentina Calabrese,[†] Matilde Forcella,[†] Paola Fusi,[†] Cristina Airoldi,[†] Carlotta Ciaramelli,[†] Jean-Marc Billod,[‡] Andra B. Schromm,[§] Harald Braun,[∥] Charys Palmer,[⊥] Rudi Beyaert,[∥] Fabio Lapenta,[#] Roman Jerala,[#] Grisha Pirianov,[⊥] Sonsoles Martin-Santamaria,[‡] and Francesco Peri*,[†]

[†]Department of Biotechnology and Biosciences, University of Milano-Bicocca, Piazza della Scienza, 2, 20126 Milano, Italy

[‡]Department of Structural & Chemical Biology, Centro de Investigaciones Biologicas, CIB-CSIC, C/Ramiro de Maeztu, 9, 28040 Madrid, Spain

[§]Division of Immunobiophysics, Research Center Borstel, Parkallee 1-40, 23845 Borstel, Germany

[∥]VIB-UGent Center for Inflammation Research, UGent Department for Biomedical Molecular Biology, Unit of Molecular Signal Transduction in Inflammation, Technologiepark 927, 9052 Ghent, Belgium

[⊥]Anglia Ruskin Cambridge University, Cambridge CB1 1PT, U.K.

[#]Department of Synthetic Biology and Immunology, Kemijski Institute, National Institute of Chemistry, Hajdrihova 19, SI-1000 Ljubljana, Slovenia

Supporting Information

ABSTRACT: The structure−activity relationship was investigated in a series of synthetic TLR4 antagonists formed by a glucosamine core linked to two phosphate esters and two linear carbon chains. Molecular modeling showed that the compounds with 10, 12, and 14 carbons chains are associated with higher stabilization of the MD-2/TLR4 antagonist conformation than in the case of the C16 variant. Binding experiments with human MD-2 showed that the C12 and C14 variants have higher affinity than C10, while the C16 variant did not interact with the protein. The molecules, with the exception of the C16 variant, inhibited the LPS-stimulated TLR4 signal in human and murine cells, and the antagonist potency mirrored the MD-2 affinity calculated from *in vitro* binding experiments. Fourier-transform infrared, nuclear magnetic resonance, and small angle X-ray scattering measurements suggested that the aggregation state in aqueous solution depends on fatty acid chain lengths and that this property can influence TLR4 activity in this series of compounds.

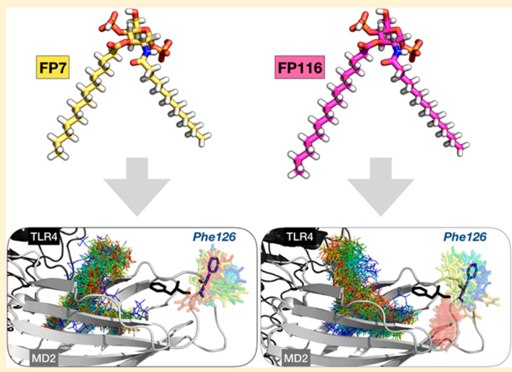

INTRODUCTION

Toll-like receptors (TLRs) are pattern recognition receptors (PRRs) that recognize pathogen-associated molecular patterns (PAMPs). TLR4 is mainly expressed on hematopoietic cells including monocytes, dendritic cells, and macrophages.[1] Lipopolysaccharide (LPS), lipooligosaccharide (LOS), and lipid A from Gram-negative bacteria are generally called endotoxin and are powerful TLR4 agonists.[2] TLR4 responds rapidly to minute amounts of circulating LPS through a multistep molecular recognition process, initiated by transfer of LPS monomers from aggregates in solution to LPS-binding protein (LBP), and subsequently to cluster to differentiation 14 (CD14) and to myeloid differentiation factor 2 (MD-2). MD-2 is associated with TLR4 in MD-2/TLR4 complexes on cell membrane. In the absence of agonist, the complex TLR4/MD-2 is in equilibrium between monomeric and dimeric species. Recent quantitative single-molecule localization microscopy (SMLM) studies[3] have shown that LPS binding to MD-2[4] displaces the equilibrium toward homodimeric complexes $(TLR4/MD\text{-}2/LPS)_2$.[3,5] The homodimer transmits the signal downstream through two distinct pathways. One pathway starts by recruitment of myeloid differentiation primary response gene 88 (MyD88) and adapter myelin and lymphocyte protein (MAL) (MyD88-dependent pathways and production of a number of pro-inflammatory proteins), the other by the activation of TIR-domain-containing adapter-inducing interferon-γ (TRIF) (MyD88-independent pathways and production of interferons).[6]

In addition to bacterial PAMPs, TLR4 can be also activated by damage-associated molecular patterns (DAMPs), endogenous agonists responsible for sterile inflammation, such as

Received: December 11, 2017
Published: March 1, 2018

DOI: 10.1021/acs.jmedchem.7b01803
J. Med. Chem. 2018, 61, 2895−2909

fibronectins,[7] saturated palmitic acid,[8] oxidized phospholipids,[9] or high-mobility group box 1 (HMGB1) protein[10] which have also been shown to activate TLR4. While different LPS chemotypes share a conserved lipid A moiety with chemical determinants that ensure optimal interaction with CD14 and MD-2 (five or six lipophilic fatty acid chains attached to a disaccharide backbone, and one or two phosphate groups), DAMPs are chemically diverse molecules, and the molecular mechanism of TLR4 activation including the role of CD14 and MD-2 in the sensing of these molecules are not entirely understood. DAMPs have been implicated in many pathologies caused by TLR4 activation including atherosclerosis,[11] rheumatoid arthritis,[12] neuroinflammation,[13] trauma,[14] and hemorrhage.[15]

These findings strongly support the idea that regulation of TLR4 activity appears as a potential target for therapeutic control of a variety of inflammatory-based diseases. Manipulation of TLR4-mediated immune responses as a potential approach for pharmacological intervention has been reported in the literature.[16] For the past few years, several TLR4 antagonists have been evaluated in preclinical studies, but only two drugs, E5564[17] (Eritoran, Eisai, Inc.) and TAK-242[18] (Takeda Biological), progressed to clinical trials for treatment of sepsis, which have been discontinued in different phases.[19,20]

Efficient and selective TLR4 antagonists with a chemical structure simpler than lipid A are the basis for development of novel TLR4 modulators. Lipid A consists of a 1,4-diphosphorylated diglucosamine backbone to which variable lengths and numbers of fatty acid (FA) acyl chains are covalently linked.[2] Lipid X (Figure 1),[21] a biosynthetic precursor of lipid A with TLR4 antagonist activity, has been considered a simplified monosaccharide scaffold for the development of novel TLR4 modulators.

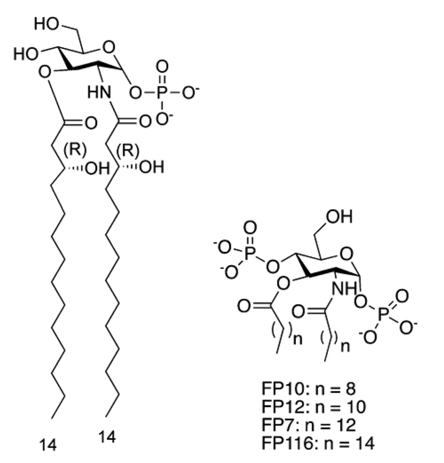

Figure 1. Chemical structures of lipid X and FP7 variants.

Our group developed the lipid X mimetic FP7,[6] a glucosamine derivative with two phosphate groups and two myristic (C14) fatty acid (FA) chains, whose design was inspired by other glucosamine-based TLR4 modulators.[22−24] FP7 is active in inhibiting in a dose-dependent way human[6] and murine[25] TLR4 activation by LPS. Some preliminary observations from nuclear magnetic resonance (NMR) experiments suggest that FP7 interact with MD-2, probably inserting FA chains into hydrophobic binding cavity.[6] This direct competition with LPS for MD-2 binding is probably reinforced by the capacity of FP7 to induce endocytosis of CD14, thus causing the absence of this receptor on the plasma membrane.[6] FP7 is active in blocking PR8 virus lethality that is mainly due to TLR4 overstimulation by endogenous DAMPs (mainly oxidized phospholipids and HMGB-1 protein) derived from viral damage to lung tissue.[25] In a proof-of-concept experiment in support of this *in vivo* mechanism, FP7 inhibited HMGB-1 activation of dendritic cells.[25] Other monosaccharide-based TLR4 modulators were developed, and structure−activity relationship (SAR) studies showed that the length of FA chain is a critical factor determining the potency of TLR4 antagonism or agonism.[22,26] The biological activity and the agonist/antagonist behavior on TLR4 of lipid A variants and other amphiphilic glycolipids including FP7 is not only determined by the interaction with MD-2 but also by the aggregation state in solution. Like LPS and lipid A, FP7 is an anionic amphiphile with a low value of CMC (9 μM).[6] Even though the CMC value of FP7 is higher than its IC_{50} (about 2 μM in HEK cells assays), equilibrium between aggregates and single molecules in solution is present in the concentration range in which FP7 is active.

It has been proposed for lipid A derivatives that the size and the 3D shape of aggregates influence the TLR4 activity, lamellar aggregates being associated with antagonism, and aggregates with nonlamellar cubic symmetry to agonism.[27,28] While the last step of ligand presentation to TLR4 and formation of the activated heterodimer $(TLR4/MD\text{-}2/ligand)_2$ is dominated by single molecule interactions between the ligand and CD14 and MD-2 receptors,[29] the early phases of endotoxin (ligand) recognition by LBP are very likely influenced by the aggregation state of the ligand.

We present here a SAR study on synthetic FP7 variants differing only for FA chains lengths (10, 12, 14, and 16 carbon atoms, Figure 1). In this study we will take into account both the interaction with MD-2 and the aggregation properties of the molecules. Additionally, we show the relationship between the chemical structure of FP7 variants with different fatty acid chains lengths and their effect on functional activity of TLR4 in different *in vitro* cell models.

RESULTS

Computational Design of FP7 Variants as Ligands of Human MD-2 and CD14. Given our previous studies on the lipid X mimetic FP7 as ligand of TLR4/MD-2 and CD14 proteins, with TLR4/MD-2 antagonist activity,[6] we were prompted to investigate the influence of the acyl chain length on the antagonist activity. To address this point, we designed three new FP7 derivatives with different fatty acid (FA) lengths: FP10 (C10), FP12 (C12), FP7 (C14), and FP116 (C16). The ability of these ligands to bind to TLR4/MD-2 complex and to CD14, compared with FP7, was initially assessed through various computational techniques.

We first docked the ligands in the binding site of CD14 using AutoDock Vina. For all the four ligands, docked poses inside the hydrophobic pocket were found. The obtained binding poses were very similar for all the ligands (Figure S1A) with also very close favorable predicted binding energies for the top poses (range from −6.5 to −5.9 kcal mol^{-1}). Therefore, the docking calculation showed that all four ligands are theoretically able to interact with CD14 inside its hydrophobic pocket and to engage in favorable interactions. In the most populated and most favorable docked poses, one phosphate group is interacting with the NH groups of Arg72 and Val73 and with the OH group of Tyr82 (Figure S1B), while the other

DOI: 10.1021/acs.jmedchem.7b01803
J. Med. Chem. 2018, 61, 2895−2909

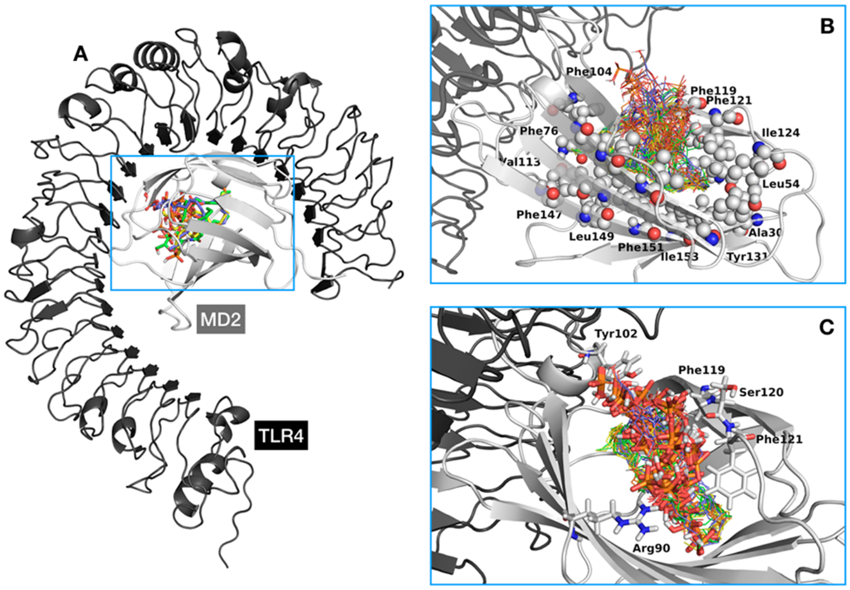

Figure 2. (A) General view of FP10 (in orange), FP12 (in yellow), FP7 (in green), and FP116 (in violet) ligands are shown docked inside TLR4/MD-2 (TLR4 is shown in black and MD-2 in gray). (B) Detail of the MD-2 hydrophobic pocket occupied by all the best docked poses for each ligand (represented as lines). Hydrophobic residues mentioned in the text as interacting with the FA chains of the ligands are represented in spheres. (C) Detail of the polar interactions of the ligands inside the TLR4/MD-2 system. Phosphate groups of the best docked poses of each ligand and the MD-2 residues with which they interact are represented in sticks.

phosphate group is exposed to the solvent. The FA chains are accommodated inside the hydrophobic pocket of CD14 interacting with aliphatic residues, mainly Ala, Val, Leu, and Ile residues and aromatic Phe49 (details are depicted in Figure S1C). The results were in agreement with previous docking studies of FP7 reported by us.[30]

We performed the docking calculations of ligands FP7, FP10, FP12, and FP116 inside the TLR4/MD-2 complex in the antagonist conformation (Figure 2). For all the compounds, favorable docked poses were found, with predicted binding energies, for the best ones, ranging from −7.8 to −6.5 kcal mol^{-1}. The polar head groups are placed at the rim of MD-2 and the FA chains go deep inside the hydrophobic pocket interacting with many hydrophobic residues, namely, Val24, Ala30, Ile32, Ile44, Ile46, Val48, Ile52, Leu54, Leu61, Ile63, Tyr65, Phe76, Leu78, Ile80, Phe104, Val113, Ile117, Phe119, Phe121, Ile124, Tyr131, Val135, Phe147, Leu149, Phe151, and Ile153 (Figure 2B).

Additionally, it was possible to observe more diversity in the predicted binding poses in TLR4/MD-2 than in the case of CD14. Results for FP7 were in agreement with those previously reported in MD-2 protein.[6] In many poses, one of the phosphate groups was close to the hydroxyl group of MD-2 Tyr102 where it establishes hydrogen bonds, and the other one was often close to MD-2 Arg90 establishing hydrogen bonds and electrostatic interactions (Figure 2C). In some docked poses, the phosphate groups were observed to interact with the backbone of residues Phe119, Ser120, and Phe121. Both phosphate groups were often placed at the rim of MD-2 where they are exposed to the solvent, in agreement with the reported X-ray crystallographic complexes of TLR4/MD-2 with glycolipids (for example, complex with Eritoran, PDB-ID 2Z65, or with lipid IVa, PDB-ID 2E59). Two different orientations were also found: type A (antagonist-like binding mode), similar to that found for lipid IVa in PDB-ID 2E59; and type B (agonist-like binding mode), similar to that found for *E. coli* lipid A in PDB-ID 3FXI (Figure S2). It is well-known that these two ligands, lipid IVa and *E. coli* lipid A, bind to TLR4/MD-2 in a different manner, one being rotated 180° compared to the other one, leading to opposed biological activities.

Selected binding poses were used as starting structures for redocking with AutoDock4 resulting in predicted binding energies ranging from −4.6 to +4.3 kcal mol^{-1}. Among the docked solutions, the best poses (from −4.6 to −2.5 kcal mol^{-1}) corresponded to binding poses very similar to those obtained with AutoDock Vina (data not shown). The narrow binding energy range did not permit to rank the ligands by predicted affinity, showing that the four ligands are putative binders of the TLR4/MD-2 system. Given that the main interactions (the polar ones) are common to the four ligands and that the MD-2 pocket is big enough to host two longer FA chains, from the docking calculations, it was not possible to clearly correlate the subtle differences in FA chain length with preferred ligand binding.

Stability of the predicted TLR4/MD-2/ligand complexes was further studied by molecular dynamics (MD) simulations. We selected two of the best binding poses for each ligand (Figure S3): one type A (antagonist-like binding pose) and one type B (agonist-like binding pose), plus two additional poses for compounds FP10 and FP7. Therefore, a total of eight 50 ns MD simulations were run. We monitored the motion of MD-2 over time and examined the root-mean-square deviation (rmsd) and rms fluctuation per residues, as well as the motion of Phe126 side chain over time (Figure S4). All the complexes showed stable ligand−receptor interactions along the MD simulation time as predicted by the docking calculations. In particular, in the MD simulation of the TLR4/MD-2/FP7 complex in the type A (antagonist-like) binding pose, the Phe126 side chain moves around its initial position staying largely exposed to the solvent in a conformation in agreement with the X-ray crystallographic antagonist conformation of MD-2 (Figure 3A).

DOI: 10.1021/acs.jmedchem.7b01803
J. Med. Chem. 2018, 61, 2895−2909

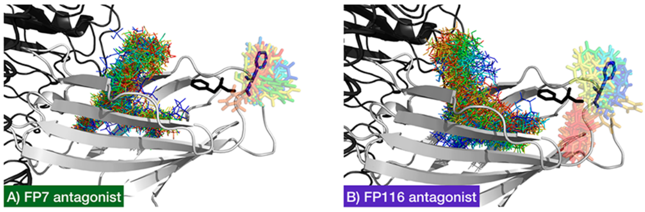

Figure 3. Superimposition of different snapshots (one for each simulated nanosecond), from the MD simulations of the TLR4/MD-2/ligand complexes, colored from blue (t = 0 ns) to red (t = 50 ns). Only ligands (as lines) and Phe126 (in sticks) are made visible. Side chains of Phe126 from the X-ray crystallographic structures have been superimposed to the snapshots to illustrate the antagonist (dark blue, PDB-ID 2E59) and agonist (black, PDB-ID 3FXI) conformations of MD-2. (A) TLR4/MD-2/FP7 complex starting from the type A binding pose (antagonist-like). (B) TLR4/MD-2/FP116 complex starting from the type A binding pose (antagonist-like).

To evaluate the relative orientation between the ligands and MD-2, we arbitrarily defined two vectors, one from the amide carbon atom to the ester and carbon atom of the ligand, and another one from the carbon of residues Pro78 to Thr105 of MD-2 (Figure S5A). The angle between these two vectors was plotted both over time and as a percentage of frames per 0.1 degree angle range (Figure S6). It was observed that none of the ligands undergoes orientation flip during the 50 ns simulations; all remain in the orientation from the docking process. Interestingly, only in the case of the TLR4/MD-2/FP116 complex with FP116 in the type A (antagonist-like) binding pose does the orientation of Phe126 side chain flip over (Figure 3B). We monitored this flipping behavior along the MD simulations, for all the ligands, by arbitrarily choosing two vectors, within MD-2, both starting from the carbon of residue Phe126 to, respectively, the phenyl C-4 atom of the same residue and the carbon of residue Ser21 (data shown in Figures S5B and S7). This observation could suggest that FP116 is not able to efficiently retain an antagonist conformation of MD-2, thus pointing to a poor antagonist capacity.

Additionally, logP values of compounds FP10, FP12, FP7, and FP116 were computationally calculated, ranging from approximately 4 to 10 with a linear distribution (Figure S8). The highest logP value was obtained for FP116 indicating a high lipophilicity that might result in low water solubility. This was in agreement with the lower acyl chain mobility as analyzed by Fourier-transform infrared (FT-IR) spectroscopy (see below). In any case, this did not interfere with the performance of the cell assays. Summarizing, the computational studies assessed the ability of ligands FP7, FP10, FP12, and FP116 to bind both CD14 and TLR4/MD-2, pointing to the long FP116 acyl chain (C16) as the maximum length bordering good

Scheme 1[a]

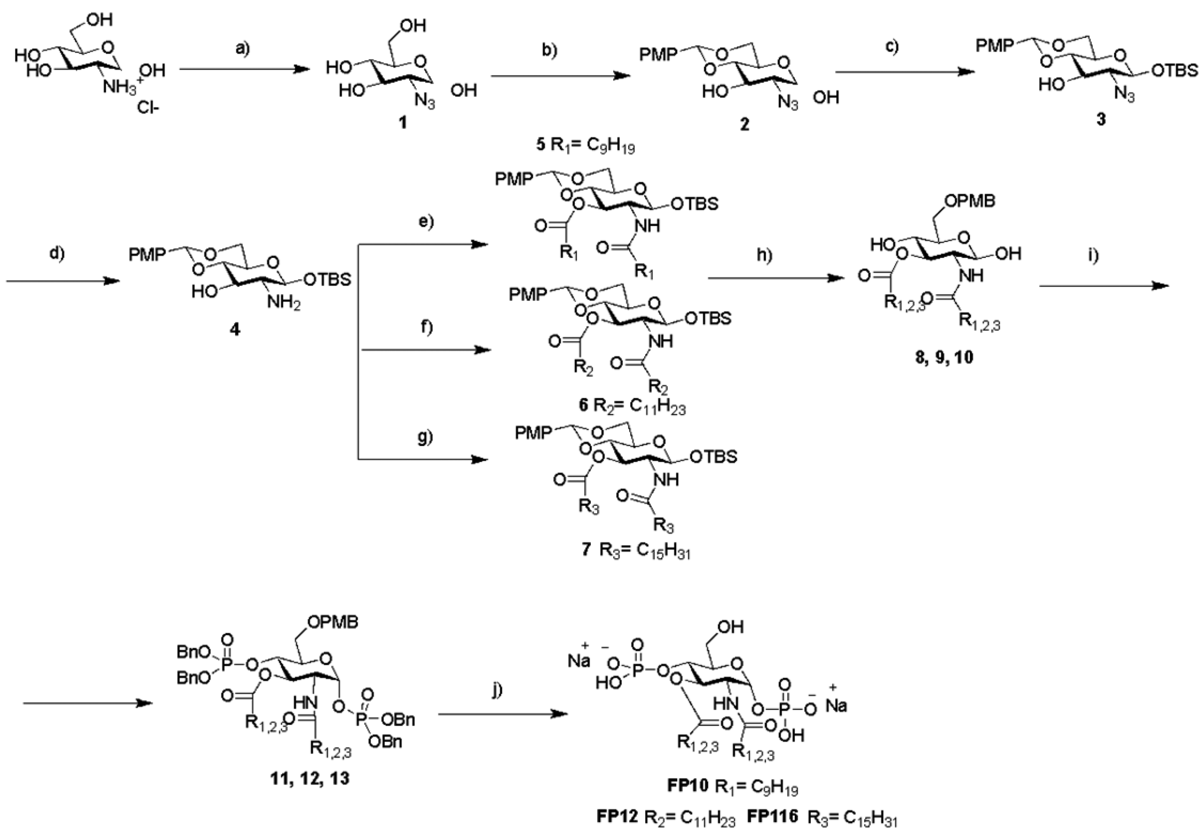

[a]Reagents and conditions: (a) $CuSO_4$, TEA, Py:H_2O, 0 °C, 30 min then TfN_3, Py, 0 °C−rt, O.N., quant.; (b) p-MeOPhCH$(OMe)_2$, CSA, DMF dry, 40 °C, 8 h, 68%; (c) TBSCl, imidazole, CH_2Cl_2 dry, rt, 1.5 h, 62%; (d) PPh_3, THF/H_2O, 60 °C, 2 h, quant.; (e) decanoic acid, EDC, DMAP, CH_2Cl_2 dry, rt, 6 h, 79%; (f) lauroyl chloride, DMAP, Py dry, 0 °C−rt, O.N., 79%; (g) palmitoyl chloride, DMAP, Py dry, rt, O.N., 75%; (h) $NaCNBH_3$, 4 Å MS, THF dry, rt, O.N., then HCl 1 M in dioxane until pH 2, 12−70%; (i) $(BnO)_2PNiPr_2$, imidazolium triflate, CH_2Cl_2 dry, rt, 30 min, then m-CPBA, 0 °C−rt, O.N., 51−56%; (j) (i) H_2, Pd/C, MeOH dry/CH_2Cl_2 dry, rt, O.N., (ii) Et_3N, (iii) IRA 120 H^+ resin, (iv) IR 120 Na^+, 84%-quant.

DOI: 10.1021/acs.jmedchem.7b01803
J. Med. Chem. 2018, 61, 2895−2909

(predicted) binding properties. The compounds were therefore synthesized and tested.

Synthesis of FP Variants. Compounds FP7, FP10, FP12, and FP116 were synthesized according to a divergent synthetic strategy starting from the common precursor **4** (Scheme 1).

Commercially available D-glucosamine hydrochloride was converted into the intermediate **4** by subsequent protection of C-4 and C-6 positions as *p*-methoybenzylidene and the anomeric (C-1) position as *tert*-butyldimethylsislyl (TBDMS) ether.[6] Intermediate **4** was then acylated in positions C2 and C3 according to three different procedures, obtaining monosaccharides **8**, **9**, and **10** with, respectively, C10, C12, and C16 carbon FA chains. Compound FP7, with C14 chains, was obtained similarly following a published procedure.[6] Regioselective *p*-methoxybenzylidene ring opening as *p*-methoxybenzyl (PMB) ether in C-6, followed by phosphorylation of free hydroxyls in positions C1 and C4, and final deprotection of PMB ethers gave final compounds as triethylammonium ions. Exchange of triethylammonium with sodium (IR120 Na^+ ion-exchange resin) followed by reverse-phase purification gave final compounds FP10, FP12, and FP116 with a purity ≥95%.

Aggregation Properties of FP Compounds. *FT-IR Studies.* The mobility of the acyl chains is an important biophysical parameter of aggregated lipids. Biological lipids typically show a temperature-dependent phase transition from a highly ordered gel (Lβ) phase of the hydrocarbon chains at low temperatures (indicated by an absorption peak around 2850 cm^{-1}) to a liquid-cystalline (Lα) phase at higher temperatures (indicated by a absorption peak around 2852 cm^{-1}). The phase transition temperature (T_c) is characteristic of the chemical structure of the lipids. The FP compounds were analyzed by FT-IR spectroscopy to determine the lipid phase in dependence of temperature. FP compounds with shorter acyl chains (FP10, C10 and FP12, C12) were found to be in a fluid Lα phase with high mobility of their acyl chains at all temperatures. FP compounds with longer acyl chains (FP7, C14 and FP116, C16) showed a biphasic behavior with a clear Lβ to Lα phase transition with T_c around 28.5 °C for FP7 and around 40.2 °C for FP116 (Figure 4). Notably, the main phase transition of FP116 at 40.2 °C occurs along a broad temperature range, and a second phase transition is observed around 65 °C. Thus, at a biological relevant temperature of 37 °C, FP10, FP12, and FP7 exhibit a fluid membrane phase, whereas FP116 is still in a rigid membrane phase and requires much higher temperatures for acyl chain melting to occur.

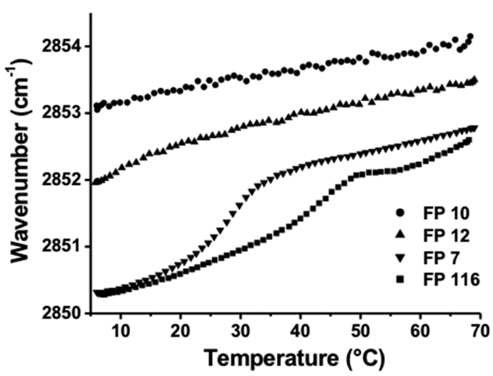

Figure 4. Acyl chain mobility of the aggregated FP compounds in dependence on temperature. The infrared absorption around wavenumbers 2850−2852 cm^{-1} corresponds to the symmetric stretching vibrations ν_s of the CH_2 groups of the acyl chains. The wavenumbers indicated were derived from the peak absorption of $\nu_s(CH_2)$ determined upon constant heating of the samples. Data are representative of two independent measurements.

NMR Studies. The comparison of the ^1H NMR spectra recorded after compound dissolution in phosphate buffer, pH 7.4, 25 °C (Figure S9) suggested a different aggregation state of the bioactive compounds in solution in the micromolar concentration range. The ^1H NMR spectrum acquired on a 100 μM FP7 sample (Figure S9A) clearly showed the presence of two sets of signals, as can be deduced by observing the spectral region between 5.5 and 5.2 ppm. In addition to a doublet of doublet and a triplet, corresponding to H1 and H3 protons (*), also two broad resonances (§) are present that can be assigned to aggregated species. This hypothesis was supported by the comparison of spectrum S9A with FP7 spectra recorded at higher concentrations, in particular 125 μM (Figure S9B) and 250 μM (Figure S9C), where the gradual decrease in sharp signal (*) intensity is associated with the increase of the broad resonance (§) ones, as expected as a consequence of FP7 aggregation. A further confirmation was achieved through the acquisition of relaxation-edited (Figure S9D) and diffusion-edited (Figure S9E) spectra, employed to partially filter out resonances from high molecular weight and low molecular weight species, respectively.[31,32] Indeed, the spectrum acquired with the CPMG sequence (Figure S9D), edited on the basis of relaxation times and thus highlighting the signals from low molecular weight species, showed a decrease of broad signal (§) intensities compared to spectrum S9C; on the contrary, in the diffusion-edited spectrum (Figure S9E), whose parameters were set up to erase resonances from low molecular weight compounds, sharp resonances (*) disappeared. We can conclude that, under our experimental condition, FP7 was present in solution as a mixture of monomer/small aggregates and higher aggregated species (micelles), whose equilibrium changes coherently to the variation of the nominal concentration of the molecule.

Instead, only one set of sharp signals was observed in the ^1H NMR spectra recorded on FP10 and FP12 solutions containing the compounds in the concentration range 100 μM to 1 mM. Representative spectra acquired on 500 μM samples are depicted in Figure S9F−H for FP10 and Figure S9I−M for FP12. Furthermore, FP10 and FP12 resonances appear considerably narrower compared to FP7 signals (Figure S9A). Collectively, these findings suggest an appreciably higher solubility of FP10 and FP12 in aqueous buffer solution and thus a lower propensity to form micelles.

A different behavior can be described for FP116. All the ^1H NMR spectra acquired on this compound present broad resonances and no sharp signals, expected for the free monomer. Thus, in the range of tested concentrations (125−500 μM), FP116 is always present in an aggregated form. Representative spectra acquired on a 250 μM FP116 sample are reported in Figure S9N−P.

SAXS Studies. Small angle X-ray scattering (SAXS) profiles were measured in dependence of temperature to obtain information on the supramolecular organization of the molecules. The data are given in the range of the scattering vectors relevant for structure assignment. All FP compounds showed isotropic scattering, indicating no preference for a predominant orientation of the aggregates. FP10 and FP12 showed diffuse symmetric scattering curves dominated by the

DOI: 10.1021/acs.jmedchem.7b01803
J. Med. Chem. 2018, 61, 2895−2909

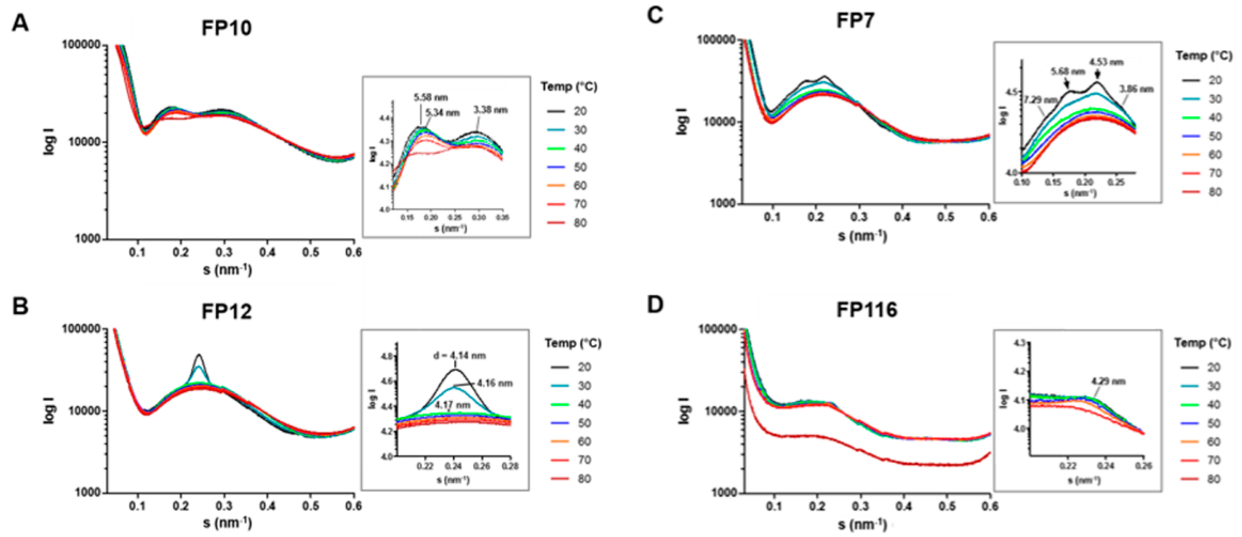

Figure 5. Small angle X-ray diffraction of aggregates in solution for FP10 (A), FP12 (B), FP7 (C), and FP116 (D). Scattering vectors are indicated for temperatures between 20 and 80 °C. Gray squares show enlargements of the relevant scattering vectors. The spacing of the diffraction maxima is indicted as $d = 1/s$ (nm).

form factor, which is characteristic for unilamellar aggregates with large interbilayer distance and probably owing to the negative surface charge of the two adjacent phosphate groups that leads to a net electrostatic repulsion of the bilayers (Figure 5). The scattering of FP10 shows two maxima at 5.58 nm and at 3.38 nm, the latter could indicate the formation of interdigitated bilayers (3.38 nm). For FP12, a single peak is observed at 20 °C (up to 35 °C, data not shown) indicating the formation of correlated multilayers with a *d*-spacing of 4.14 nm, which is also consistent with the formation of an interdigitated bilayer structure. In contrast, FP7 does show a different and more complex scattering pattern, which indicates the occurrence of a nonlamellar structure. The spacing relationship exhibits clear similarity with cubic structures with a space group relationship of aQ 12.7 nm (not visible), $aQ/\sqrt{3}$ (7.29 nm), $aQ/\sqrt{5}$ (5.68 nm), $aQ/\sqrt{8}$ (4.53 nm), and $aQ/\sqrt{11}$ (3.86 nm), agreeing most likely with space group Q_{212}. The tendency to a nonlamellar structure of FP7, however, could explain the slightly lower antagonistic activity of FP7 compared to FP12. In contrast to the above FP compounds, FP116 showed very weak scattering intensities, hardly displaying a form factor, which can be explained by a much lower solubility observed for the FP116 preparation and supports the results obtained by NMR.

Binding to MD-2. *Expression, Purification, and Activity of hMD-2.* Recombinant human MD-2 (hMD-2) was used in *in vitro* binding experiments. The functionality of this protein is a crucial prerequisite to obtain reliable results representative of specific, high-affinity molecular recognition of ligands.[33] Recombinant hMD-2 was expressed in *E. coli*, *Pichia pastoris*, and mammalian HEK293 cells. hMD-2 from different hosts was tested for its activity by incubating HEK/hTLR4 cells with a mixture of recombinant hMD-2 and LPS (100 ng/mL). The TLR4-dependent IL-8 secretion by HEK/hTLR4 cells is indicative of functional MD-2. Figure 6 shows the lowest concentration of MD-2 required for maximum activation of TLR4 (quantified by IL-8 production), for each of the different expressed and purified hMD-2 proteins. hMD-2 produced and purified from HEK293T displayed the highest activity in stimulating the LPS/TLR4 inducible reporter at a concentration of 12 nM, followed by the hMD-2 expressed and

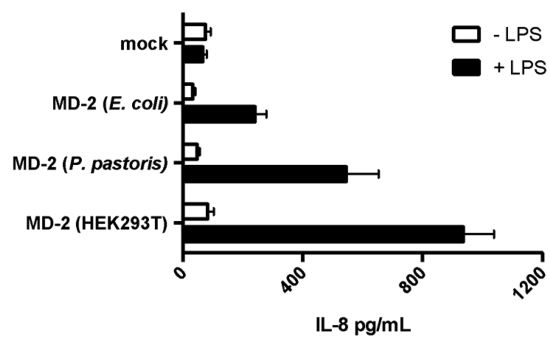

Figure 6. Activity of hMD-2 expressed in different hosts. The figure shows the maximum activation of TLR4 (quantified by IL-8 production) at the lowest concentration of hMD-2 under the different expressed conditions (bacteria 245 nM, yeast 15 nM, and mammalian 12 nM). Results are mean ± SEM from three parallels representative of at least three independent experiments.

purified from *P. pastoris* with its highest biological activity obtained at a concentration of 15 nM. Finally, hMD-2 purified from *E. coli* gave the lowest IL-8 production at the concentration of 245 nM (Figure 6).

The difference in activity of hMD-2 expressed in different hosts most likely reflects minor differences in protein folding and/or glycosylation.[34,35] The higher expression yield and the good activity prompted us to use hMD-2 from *P. pastoris* in *in vitro* binding experiments with synthetic compounds.

Binding studies were carried out by means of fours different techniques: two ELISA-type plate-based assays with immobilized protein, a fluorescence displacement assay, and surface plasmon resonance (SPR).

ELISA Competition Experiments with Anti-hMD-2 Antibody. Direct binding of LPS, FP7, FP10, and FP12 to MD-2 was determined using a monoclonal antibody that binds to free hMD-2 but not to hMD-2 bound to LPS.[36] Monoclonal mouse anti-hMD-2 (9B4) antibody specifically binds to an epitope close to the rim of the LPS-binding pocket of hMD-2, available for recognition by the antibody only when the hMD-2 pocket is empty.

DOI: 10.1021/acs.jmedchem.7b01803
J. Med. Chem. 2018, 61, 2895−2909

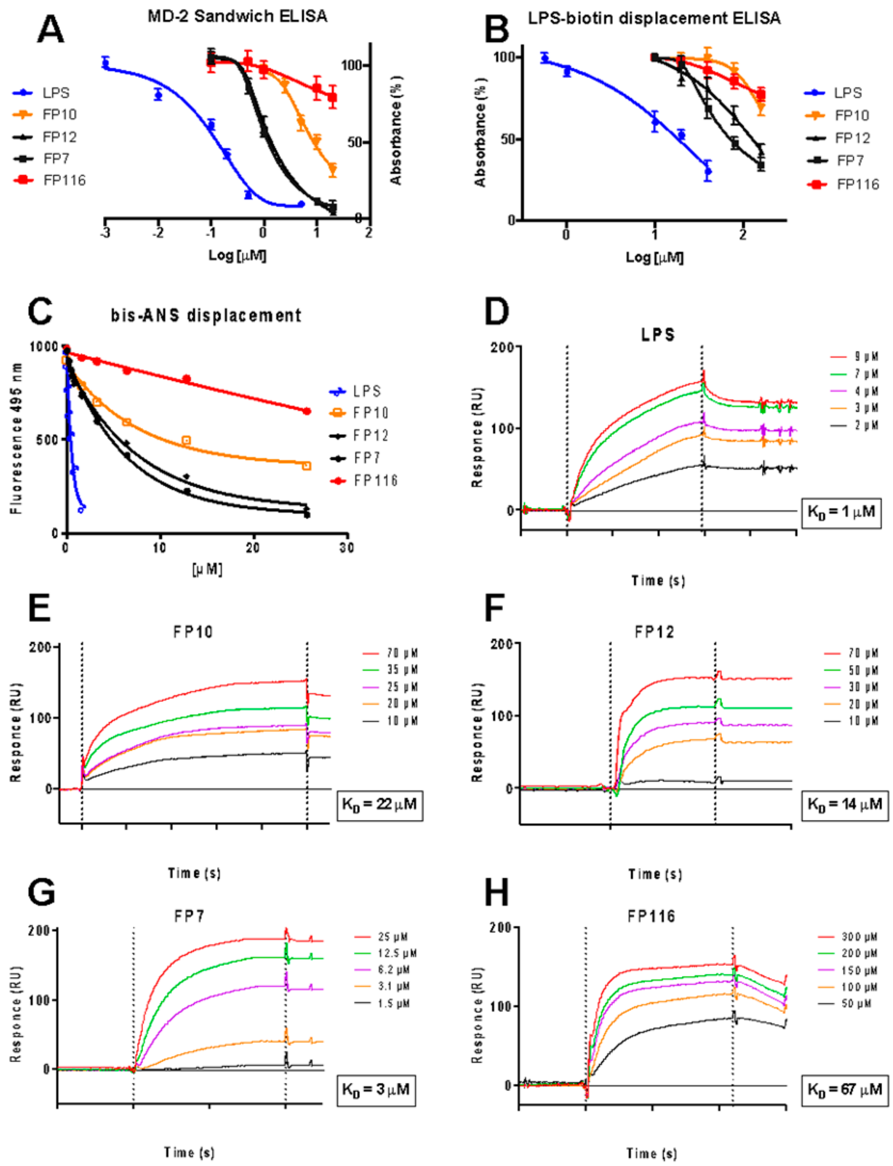

Figure 7. Cell-free binding studies on purified\ hMD-2 receptor. (A) LPS, FP7, FP10, and FP12 prevent anti-human MD-2 monoclonal antibody binding in a dose-dependent manner. (B) LPS, FP7, FP10, FP12, and FP116 activity in competing with biotin-LPS for hMD-2 binding. (C) Fluorescence measurements show that LPS, FP7, FP10, and FP12 dose-dependently inhibit the binding of bis-ANS to MD-2. (D−H) SPR analysis shows direct interaction between LPS, FP10, FP12, FP7, and FP116 and MD-2; K_D values are reported. Results are mean ± SEM from three parallels representative of at least three independent experiments.

This assay detected a decrease in binding to MD-2 in the presence of LPS (Figure 7A), similar to that previously reported.[37] A dose-dependent inhibition of antibody/MD-2 interaction was observed when adding FP7 and FP12, with a 90−95% decrease in binding obtained at concentrations of FP7 and FP12 of 20 μM (Figure 7A). A 70% decrease in binding to hMD-2 was obtained with 20 μM of FP10 (Figure 7A), and a 20% decrease was obtained with 20 μM of FP116 (Figure 7A). These data showed that, while FP7 and FP12 bind hMD-2 with high affinity, FP10 and FP116 are less potent ligands.

ELISA Displacement Experiment with Immobilized hMD-2 and Biotinylated LPS. The ability of FP compounds to displace LPS from the pocket of hMD-2 was assessed by an ELISA plate-based assay. The synthetic molecules were added at increasing concentration to hMD-2, which was already incubated with biotinylated LPS. FP7 and FP12 were able to displace biotin-LPS from hMD-2 in a dose-dependent manner, with the highest displacement of 60−65% obtained at a concentration of 160 μM (Figure 7B). FP10 and FP116, at a concentration of 160 μM, gave a displacement of biotin-LPS of 20−30% (Figure 7B). As a control, LPS at a concentration of 40 μM gave the highest displacement of biotin-LPS of 70% (Figure 7B).

Fluorescence Displacement Assay. It has been previously shown that the fluorescent probe 1,1′-Bis(anilino)-4,4′-bis (naphthalene)-8,8′ disulfonate (*bis*-ANS) binds to MD-2 and is displaced by LPS.[38] bis-ANS presumably binds the same MD-2 binding site as lipid A and of other lipid A-like ligands. TLR4 ligands interacting with MD-2 in a lipid A-like manner are supposed to compete with bis-ANS and displace it from MD-2. LPS, FP7, FP10, and FP12 caused a concentration-dependent decrease of bis-ANS fluorescence, indicating competitive binding of FP7, FP10, and FP12 to hMD-2 (Figure 7C). FP116 induces only a modest decrease of bis-ANS fluorescence

DOI: 10.1021/acs.jmedchem.7b01803
J. Med. Chem. 2018, 61, 2895−2909

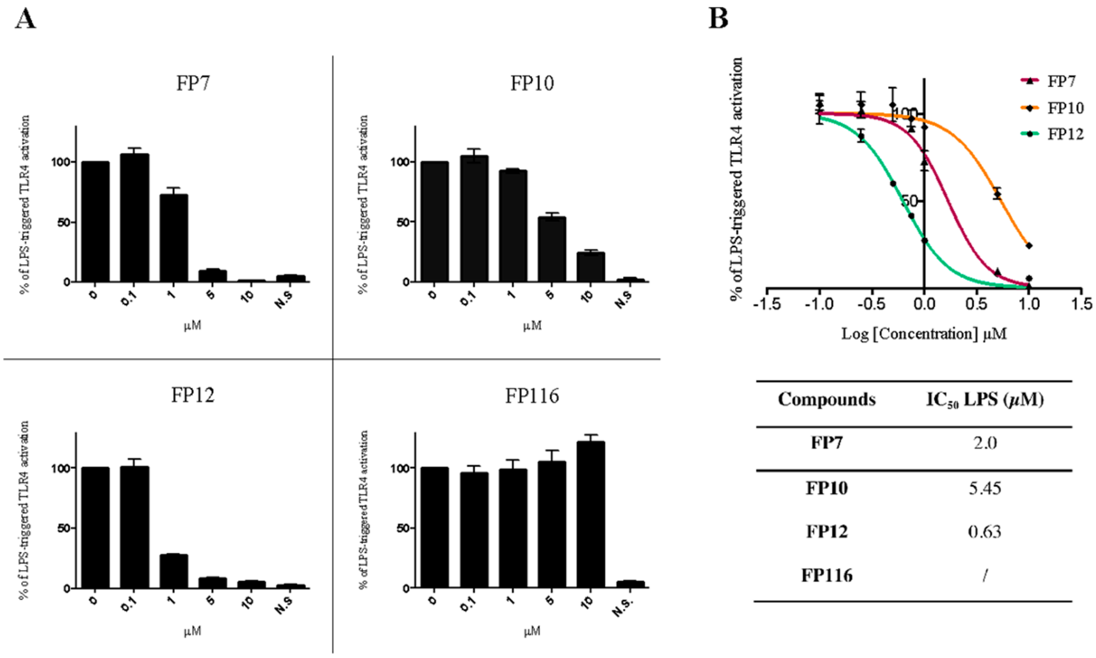

Compounds	IC_{50} LPS (μM)
FP7	2.0
FP10	5.45
FP12	0.63
FP116	/

Figure 8. Dose-dependent inhibition of LPS-triggered TLR4-dependent NF-kB activation in HEK-Blue hTLR4 cells by compounds FP7, FP10, FP12, and FP116. (A) HEK-Blue hTLR4 cells were preincubated with the indicated concentrations of compounds FP7, FP10, FP12, and FP116 and stimulated with LPS (100 ng/mL) after 30 min. Data were normalized to stimulation with LPS alone and expressed as the mean percentage ± SEM of at least three independent experiments. (B) Dose−response curves for compounds FP7, FP10, and FP12 in inducing the TLR4-dependent NF-κB reporter activity. Concentration−effect data were fitted to a sigmoidal four-parameter logistic equation to determine IC_{50} values. Data points represent the mean of percentage ± SEM of at least three independent experiments.

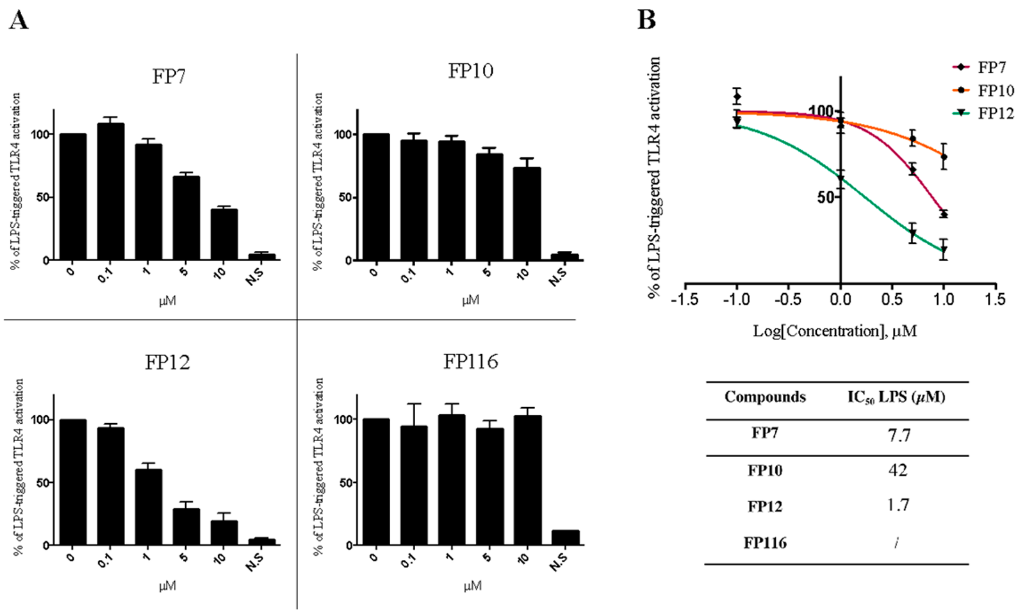

Compounds	IC_{50} LPS (μM)
FP7	7.7
FP10	42
FP12	1.7
FP116	/

Figure 9. Activity of compounds FP10, FP12, and FP116 on RAW-Blue cells. (A) RAW-Blue cells were preincubated with increasing concentrations of synthetic compounds and then stimulated with LPS (10 ng/mL, after 30 min). Data were normalized to the response to LPS and expressed as the mean percentage ± SEM of at least three independent experiments. (B) Dose-dependent inhibition curves of compounds FP7, FP10, and FP12. IC_{50} values in the table on the bottom. Concentration−effect data were fitted to a sigmoidal four-parameter logistic equation to determine IC_{50} values. Data points represent the mean of percentage ± SEM of at least three independent experiments.

at the tested concentrations (Figure 7C), thus confirming that the lack of activity on cells could be related to low affinity binding of this molecule to hMD-2.

Surface Plasmon Resonance (SPR) Analysis. SPR data with immobilized hMD-2 showed direct interaction of the receptor with LPS (control) and with the tested synthetic compounds. K_D values derived from sensorgram analysis were 3, 13.7 , 22, and 66.8 μM for FP12, FP7, FP10, and FP116, respectively (Figure 7E−H). SPR experimental curve optimal fitting was obtained by assuming 1:1 ligand/MD-2 binding stoichiometry.

Together, the results obtained from these *in vitro* cell-free studies clearly indicate that FP7, FP10, FP12, and FP116

DOI: 10.1021/acs.jmedchem.7b01803
J. Med. Chem. 2018, 61, 2895−2909

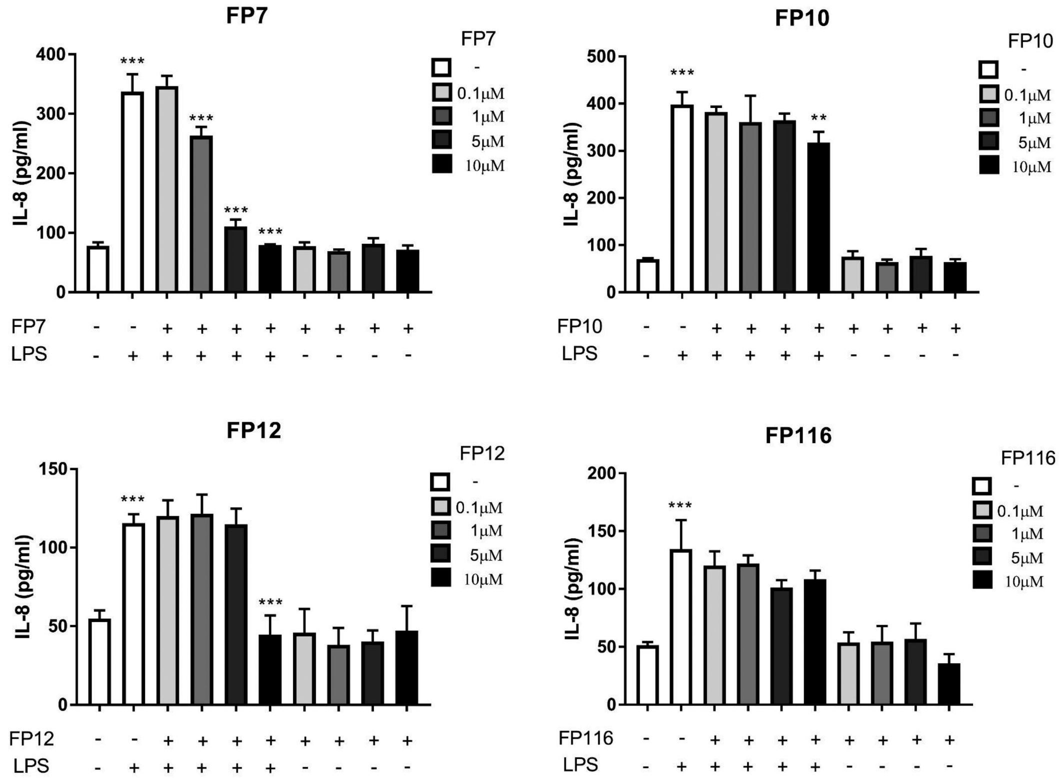

Figure 10. Effect of FP variants on LPS/TLR4 induced production of IL-8 in THP-1 cells. THP-1 cells were pretreated with FP variants (0−10 μM) for 1 h prior to LPS exposure. Cells were then left to incubate 16 h further in the presence or absence of LPS (100 ng/mL). IL-8 production was measured by ELISA. Results are displayed as mean concentration ± SD of three independent experiments. Significant results are indicated as **P* > 0.05, ***P* > 0.01, ****P* > 0.001 for LPS vs control and LPS vs FPs treated samples (ANOVA).

directly interacted with MD-2, with the same order of potency found in human and murine cell experiments FP12(C12) > FP7(C14) > FP10(C10) ≫ FP116(C16).

Cell Experiments. *Modulation of LPS-Stimulated TLR4 Signaling in HEK-Blue Cells.* In order to evaluate the influence of the fatty acid length on the TLR4 antagonist activity, molecules FP10, FP12, FP7, and FP116, constituting the homologous series with fatty acid chain lengths C10, C12, C14, and C16, were first tested on HEK-Blue hTLR4 cells. These cells are engineered to stably express the human receptors of the LPS recognition complex (hTLR4, hMD-2, and hCD14) and a reporter gene (SEAP) placed under the control of two TLR4-dependent transcription factors (NF-κB and AP-1). Results from MTT assay revealed that all compounds did not have a negative effect on cell viability at the concentration of 10 μM used in experiments (Figure S10). FP7, FP10, and FP12, but not FP116, inhibited in a concentration-dependent manner the TLR4 signaling in HEK-Blue cells (Figure 8). FP7 displayed the expected antagonistic activity.[6] FP10 and FP12 showed IC_{50} respectively higher (5.45 μM) and lower (0.63 μM) than FP7 (2.0 μM) (Figure 8B). These results demonstrated the efficacy of fatty acid chains lengths (C8, C10, and C12) of FP7 variants to negatively modulate TLR4 signaling in HEK-Blue cells, the order of activity being FP12(C12) > FP7(C14) > FP10(C10) ≫ FP116(C16).

Modulation of LPS-Stimulated TLR4 Signaling in Murine Macrophages. Several TLR4 modulators mimicking lipid A have different effects on human and murine TLR4. In certain cases when passing from murine to human TLR4/MD-2/CD14 system the observed agonistic effect switched to antagonistic effect of the compound of interest.[39] The species specificity is due to differences between hMD-2 and mMD-2 binding regions that induce different positioning of the same ligand, thus causing different activity and, in some cases, switch from agonism to antagonism. In this experiment, we aimed to investigate the effect of glucosamine derivatives in murine RAW-Blue macrophages. These cells are derived from RAW 264.7 and possess the same reporter gene present in HEK-Blue hTLR4 cells (SEAP). We first verified the capacity of FP compounds to stimulate the TLR4 response in RAW-Blue cells, and we found all molecules inactive (Figure S11). When administrated before LPS, FP7, FP10, and FP12 were active in inhibiting TLR4-dependent NF-κB activation in RAW-Blue macrophages (Figure 9A,B). Similarly to what happened in the case of human HEK cells, FP116 turned out to be inactive as antagonist. Notably, FP12 was the most active antagonist compound (IC_{50} = 1.7 μM). The activity order of the tested compounds was found to be the same than in human HEK cells: FP12(C12) > FP7(C14) > FP10(C10) ≫ FP116(C16).

Effect of FP Variants on LPS-Induced TLR4 Signaling in THP-1 Cells. Haematopoietic TLR4 has been shown to play a critical role in any stage of the inflammatory process. Furthermore, immune competent cells use TLR4 signaling to sense danger molecules and produce proinflammatory proteins that initiate and amplify the inflammatory process. To test the potential of FP variants to modulate TLR4 signaling pathways, we utilized THP-1 cells as an *in vitro* model. Initially, we evaluated the effect of FP variants on THP-1 cell viability. THP-1 cells were exposed to different concentrations of FP variants (0−10 μM) in the presence or absence of LPS (100 ng/mL) for up to 24 h. Results from MTT assay demonstrated that FP variants/LPS did not affect cell viability (Figure S12).

DOI: 10.1021/acs.jmedchem.7b01803
J. Med. Chem. 2018, 61, 2895−2909

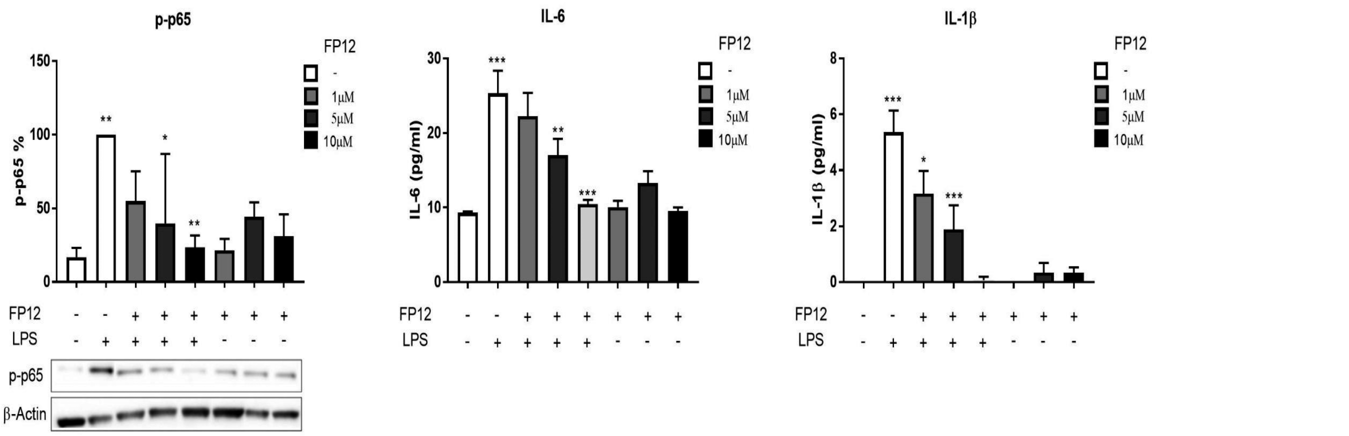

Figure 11. FP12 negatively regulates p65 NF-κB phosphorylation and production of IL-6 and IL-1β in THP-1 cells. THP-1 cells were pretreated with compound FP12 (0−10 μM) for 1 h prior to LPS exposure. Cells were then left to incubate 1 and 16 h further in presence or absence of LPS (100 ng/mL). p65 NF-κB phosphorylation was determined in cell lysates using Western blot analysis, and cytokine production was measured by ELISA after 16 h of LPS exposure, respectively. Results are displayed as mean concentration ± SD of three independent experiments. Significant results are indicated as *P > 0.05, **P > 0.01, ***P > 0.001 for LPS vs control and LPS vs FP12 treated samples (ANOVA).

To determine the effect of FP variants on TLR4 signaling, next we analyzed IL-8 expression, a well-known TLR4-dependent proinflammatory cytokine produced in THP-1 cells in response to LPS. ELISA results clearly demonstrated the potential of FP7 and FP12 at 10 μM to inhibit LPS driven IL-8 production (Figure 10). In contrast, FP10 and FP116 had a modest or nonsignificant impact on IL-8 expression, respectively (Figure 10). We have demonstrated that FP7 exerted a negative effect on TLR4 signaling in different cell types (unpublished data). Following on from comparative analysis based on TLR4-dependent IL-8 expression and tendency on the binding affinity with MD-2 of FP7 variants, we found that the structural modification of FP12, but not FP10 and FP116, is related to antagonistic activity of the compound. In support to this notion, we further investigated the ability of FP12 to modulate second messengers in TLR4 signaling. Immunoblotting data revealed that FP12 significantly downregulated p65 NF-κB phosphorylation that was associated with a strong inhibition of the expression of additional TLR4-dependent cytokines, such as IL-6 and IL-1β in a dose-dependent manner (Figure 11). These data clearly demonstrate that FP12 is a potent negative regulator of TLR4 signaling in THP-1 cells.

■ DISCUSSION AND CONCLUSIONS

The homologous series of FP glycolipids with fatty acid chain lengths varying from 10 to 16 carbon atoms was rationally designed as MD-2 ligands and synthesized.

In a first set of *in vitro* experiments, we aimed at studying the SAR of these molecules in binding experiments with functional hMD-2. For this purpose, hMD-2 expressed in yeast (*P. pastoris*) was used because it showed higher activity in responding to LPS stimulus than bacterial (*E. coli*) MD-2 and was produced with higher yields than MD-2 from mammalian (HEK) cells. Four different binding experiments between synthetic compounds and h-MD-2 were carried out. These were competition (displacement) experiments in which the synthetic glycolipids compete with biotin-LPS, with the fluorescent MD-2 ligand bis-ANS, and with anti-MD-2 antibody for MD-2 binding. SPR measurements allowed to analyze directly the binding between synthetic glycolipids and MD-2. All binding experiments consistently provided the same order of affinity among hMD-2 and synthetic molecules: FP12(C12) > FP7(C14) > FP10(C10) > FP116(C16).

The biological activity was then assessed on cells: when provided alone, the synthetic FP compounds did not display any TLR4 agonist activity in human and murine cells. On the contrary, when administrated with LPS, the molecules with 10, 12, and 14 carbon chains (respectively, FP10, FP12, and FP7) were active in blocking LPS/TLR4 signal (antagonism) in human and murine cells, while the molecule with 16 carbons (FP116) showed very weak or no activity. The order of activity of FP variants as TLR4 antagonists was confirmed in human (HEK-TLR4 and THP-1) and murine (RAW macrophages) cells. The molecules with 10, 12, and 14 carbon chains seem to be nonspecies-specific TLR4 antagonists because these compounds are active in both human (HEK and THP-1) and murine cells, with higher potency in human ones. The compound with higher biological activity was FP12, with 12 carbons, followed by FP7 and FP10 with 14 and 10 carbons, while FP116 with 16 carbons showed very weak or no activity in cell models.

The variation of compounds' functional activity was related to the number of carbon atoms of the aliphatic chains, which could be described by a bell-shaped curve with a maximum at C12. This is a common structure−activity trend that is found in a number of series of homologous compounds in medicinal chemistry and can be explained in terms of docking within the binding pocket of the pharmacological target (as it exists an optimal number of carbon atoms that can be accommodated into the pocket) and also in terms of variation of solubility and bioavailability (when the chain length is too long the solubility decreases and also the biological activity). Thus, the difference of TLR4 functional activity of FP monosaccharides related to FA chain length can be explained in terms of their interaction with MD-2(/TLR4) and/or by their aggregation properties in a solution.

The docking and MD simulation studies have shown that FP10, FP7, and FP12 would accomplish optimal binding properties, while FP116 could be bordering the limits of the maximum length compatible with a proper MD-2 binding. Although MD-2 pocket is able to host up to five FA chains, the highly long and flexible C16 acyl chains present in FP116 seem to point to less efficient ability to interact with TLR4/MD-2 in

DOI: 10.1021/acs.jmedchem.7b01803
J. Med. Chem. 2018, 61, 2895−2909

an antagonistic binding mode, given that the required exposed conformation of Phe126 side chain could be jeopardized.

Additionally, calculated logP values for the FP variants point to a very high lipophilicity for FP116, maybe affecting the aggregation properties in solution.

Taken together, these data strongly suggest that the mechanism of TLR4 antagonism of that class of compounds is mainly based on the competition with LPS (or other ligands, as bis-ANS) in the binding to the MD-2/TLR4 complex.

Interestingly, an identical order of activity on TLR4 has been found in a series of monosaccharide TLR4 agonists, the Gifu Lipid As (GLA), and the following order of potency in inducing the production of TNF-α in murine cells was detected: C12 > C14 > C10 ≫ C16.[22] Also in the case of GLA compounds, with three FA chains and one phosphate in C-4 position, the C12 and C14 variants were the most active ones, C10 was less active, and C16 was inactive. Similarly to FP compounds, GLA is more active on murine than on human cells.[22] However, the authors did not provide any evidence or explanation about the link between TLR4 activity of monosaccharide and FA chain length.

Regarding the aggregation properties, some important differences among FP compounds were detected by FT-IR analysis in solution. These measurements showed marked variations in acyl chain fluidity of aggregated FP compounds depending on the chemical structure. The phase transition temperature T_c exhibits a clear inverse correlation with the length of the acyl chains with T_c C16 ≫ T_c C14 > T_c C12 > T_c C10. Of note, this behavior results in marked differences at the biologically relevant temperature of 37 °C, where FP10, FP12, and FP7 are in a fluid membrane phase, whereas FP116 is still in a rigid membrane phase and requires much higher temperatures for acyl chain melting to occur. The occurrence of a very broad phase transition at temperatures above 37 °C and occurrence of a second phase transition at higher temperature as observed for FP116 were also found for inactive glucosamine monosaccharide GLA compounds.[40] Differences in phase behavior have also been shown for the TLR4 ligands lipid A and LPS. The antagonistic tetraacylated synthetic compound 406 is highly fluid at 37 °C, whereas the biologically active hexaacylated compound 506 and LPS Re have phase transition temperatures above 37 °C.[41] The fluidity state of the acyl chains in aggregated glycolipids is thus not an exclusive determinant of inflammatory or antagonistic activity of chemically different compounds. It is rather a modifying parameter of biological activity by affecting aggregate properties such as hydrophobic thickness, packing density, and aggregate stability. NMR and SAXS analysis revealed striking differences in aggregate formation of FP compounds, which are likely to explain differences in their biological activity. Concentration-dependent NMR analysis of the two most antagonistic compounds FP12 and FP7 revealed aggregation of FP7 (C14) at much lower concentrations than FP12 (C12), reflecting further differences in the biophysical state and bioavailability of these compounds. Aggregate structures resolved by SAXS analysis provided evidence for lamellar bilayer structures for FP10 and FP12, which are associated with antagonistic activity; for FP7, a tendency for nonlamellar structures was determined. Considering the crucial role of lipid supramolecular aggregate structure for the presentation to LPS receptor molecules, the different aggregate structures observed by SAXS might explain the slightly lower antagonistic activity of FP7 compared to FP12 in some biological systems.

The present study provides structural and functional biological data demonstrating the ability of novel FP variants to negatively regulate TLR4 signaling in different cell model systems. Having shown the strong potential of FP12 to modulate second messenger activation and various end points of TLR4 signaling pathways including its lack of toxicity, this study supports the idea of further drug development of FP12 as a lead compound in preclinical and clinical studies for pharmacological intervention of inflammatory-based diseases.

■ EXPERIMENTAL SECTION

Computational Studies. *Structure Construction and Refinement.* The 3D structures of ligands FP10, FP12, FP7, and FP116 were built with PyMOL[42] using 6YA monosaccharide found in the GLYCAM database (http://glycam.org) as a template. The 3D coordinates of human TLR4/MD-2 model in the antagonist conformation is reported elsewhere.[43]

Parameters Derivation. The parameters needed for MD simulations were obtained using the standard Antechamber procedure in Amber14.[44] Briefly, ligand structures, already refined at the AM1 level of theory, were optimized, and their atomic partial charges were calculated with Gaussian09/e1[45] at the Hartree−Fock level (HF/6-31G* Pop = MK iop(6/33 = 2), iop(6/42 = 6)), then the partial charges were derived and formatted for AmberTools15 and Amber14 with Antechamber, assigning the general AMBER force field (GAFF) atom types. Later, the atom types of the atom constituting the saccharide ring were changed to the GLYCAM force field atom types.[46] The GAFF parameters for the phosphate group were modified as shown in the Supporting Information.

Docking Calculations of Ligands FP10, FP12, FP7, and FP116. The Gasteiger charges were computed within the AutoDockTools 1.5.6 program,[47] and the nonpolar hydrogens were merged for all the ligands, the human TLR4/MD-2 antagonist model, and human CD14 (PDB-ID 4GLP). AutoDock VINA 1.1.2 was used for the docking of the ligands, and AutoDock 4.2 was used to redock the best-predicted binding poses. In AutoDock 4.2, the Lamarckian evolutionary algorithm was chosen, and all parameters were kept default except for the number of genetic algorithm runs, which was set to 200 to enhance the sampling. AutoDockTools 1.5.6 was used to assign the Gasteiger−Marsili empirical atomic partial charges to the atoms of both the ligands and the receptors. The structure of the receptors was always kept rigid, whereas the structure of the ligand was set partially flexible by providing freedom to some appropriately selected dihedral angles. Regarding the docking boxes, spacing was set to the default value of 1 Å for VINA, and 0.375 Å for AutoDock. For human CD14 structure, the size of the box was set to 33.00 Å in the *x*-axis, 33.75 Å in the *y*-axis, and 33.75 Å in the *z*-axis, and the center of the box was located equidistant to the center of mass of residues Phe69, Tyr82, and Leu89. For the human TLR4/MD-2 system, the size of the box was set to 33.00 Å in the *x*-axis, 40.50 Å in the *y*-axis, and 35.25 Å in the *z*-axis, and the center of the box was located equidistant to the center of mass of residues Arg90 (MD-2), Lys122 (MD-2), and Arg264 (TLR4).

Molecular Dynamics (MD) Simulations. Selected docked complexes were submitted to MD simulations for 50 ns in Amber14 suite. All the complexes followed the same procedure. First, the system is submitted to 1000 steps of the steepest descent algorithm followed by 7000 steps of the conjugate gradient algorithm. A 100 kcal·mol^{-1}·A^{-2} harmonic potential constraint is applied on both the proteins and the ligand. In the subsequent steps, the harmonic potential is progressively lowered (respectively to 10, 5, and 2.5 kcal·mol^{-1}·A^{-2}) for 600 steps of the conjugate gradient algorithm each time, and then the whole system is minimized uniformly. Next, the system is heated from 0 to 100 K using the Langevin thermostat in the canonical ensemble (NVT) while applying a 20 kcal·mol^{-1}·A^{-2} harmonic potential restraint on the proteins and the ligand. Finally, the system is heated up from 100 to 300 K in the isothermal−isobaric ensemble (NPT) under the same restraint condition as the previous step, followed by a simulation for 100 ps with no harmonic restraint applied. At this point, the system is ready for the production run, which is performed using the Langevin

DOI: 10.1021/acs.jmedchem.7b01803
J. Med. Chem. 2018, 61, 2895−2909

thermostat under NPT ensemble, at a 2 fs time step. All production runs were performed for 50 ns.

LogP Calculations. LogP values of FP10, FP12, FP7, and FP116 were calculated within the Maestro package.[48]

Chemistry. *General.* The reactions were carried out under a nitrogen atmosphere. TLC was performed using prepared plates of silica gel (Merck 60 F254 on aluminum) and revealed using UV light or staining reagents (H_2SO_4 (5% in EtOH), ninhydrin (5% in EtOH), basic solution of $KMnO_4$ (0.75% in H_2O), molibdate solution (molybdatophosphorus acid and Ce(IV) sulfate in 4% sulfuric acid). ^1H NMR (400 MHz) and ^{13}C NMR spectra (100 MHz) were recorded on a Varian spectrometer using partially deuterated solvents as internal standards. Purity of final compounds was ≥95% as assessed by quantitative NMR analysis. Reaction conditions and compound characterization are described in the Supporting Information.

HEK-Blue hTLR4 Cells Assay. HEK-Blue hTLR4 cells (InvivoGen) were cultured according to manufacturer's instructions. Briefly, cells were cultured in DMEM high glucose medium supplemented with 10% fetal bovine serum (FBS), 2 mM glutamine, antibiotics, and 1× HEK-Blue Selection (InvivoGen). Cells were detached using a cell scraper, counted, and seeded in a 96-well multiwell plate at a density of 4×10^4 cells per well. After overnight incubation (37 °C, 5% CO_2, 95% humidity), supernatants were replaced with new medium supplemented by the compound to be tested dissolved in water or DMSO−H_2O (1:1). After 30 min of preincubation, cells were stimulated with 100 ng/mL LPS from *E. coli* O55:B5 (Sigma-Aldrich) and incubated overnight. The SEAP-containing supernatants were collected and incubated with *para*-nitrophenylphosphate (pNPP) for 2−4 h in the dark at room temperature. The well's optical density was determined using a microplate reader set to 405 nm. The results were normalized with positive control (LPS alone) and expressed as the mean of percentage ± SEM of at least three independent experiments.

RAW-Blue Cells. Raw-Blue cells (InvivoGen) were cultured according to the manufacturer's instructions. Briefly, cells were cultured in DMEM high glucose medium supplemented with 10% fetal bovine serum (FBS), 2 mM glutamine, 100 μg/mL Normocin (InvivoGen), and 200 μg/mL Zeocin (InvivoGen). Cells were detached using a cell scraper, and the cell concentration was estimated by using Trypan Blue (Sigma-Aldrich). The cells were diluted in DMEM high glucose medium supplemented as described before and seeded in 96-well multiwell plate at a density of 6×10^4 cells per well in 200 μL. After overnight incubation (37 °C, 5% CO_2, 95% humidity), supernatant was removed, and cell monolayers were washed with warm PBS, treated with increasing concentrations of compounds dissolved in DMSO−H_2O (1:1), and diluted in DMEM. After 30 min, cells were stimulated with 10 ng/mL of LPS from *E. coli* O55:B5 (Sigma-Aldrich) for 16 h. The supernatants were collected and incubated with pNPP for 2−4 h in the dark at room temperature. The optical density of wells was determined using a microplate reader set to 405 nm. The results were normalized with positive control (LPS alone) and expressed as the mean of percentage ± SEM of at least three independent experiments.

THP-1 Cells. THP-1 cells were cultured in RPMI (+10% heat inactivated fetal bovine serum (HiFPS), +1% glutamine, +1% penicillin/streptamycin). Cells were split three times weekly and maintained at a density of 0.3×10^6 cells/mL. For experimental procedures, THP-1 was used at a density 0.5×10^6 cells/mL, 100 L/well (96 wells), and 3 mL/well (six wells) plates, respectively. All cells were pretreated with FP7 variants (0−10 M) for 1 h, then exposed to LPS (100 ng/mL) for 1 or 16 h.

MTT Cell Viability Assay. HEK-Blue hTLR4 cells were grown in DMEM supplemented with 10% FBS, 2 mM glutamine, and antibiotics. Cells were seeded in 100 μL of DMEM without Phenol Red at a density of 4×10^4 cells per well and incubated overnight (37 °C, 5% CO_2, 95% humidity). Cells were treated with the higher dose of compound used in the previous experiments and incubated overnight. MTT solution (5 mg/mL in PBS) was added to each well, and after 3 h incubation, 0.1 N HCl in 2-propanol solution was used to dissolve formazan crystals. Formazan concentration was determined by measuring the absorbance at 570 nm. The results were normalized with untreated control (PBS) and expressed as the mean of percentage ± SEM of three independent experiments.

Preparation of Recombinant hMD-2 in Escherichia coli and Purification. hMD-2 was produced in *E. coli* as described previously,[49] analyzed by SDS−PAGE, and its biological activity tested on 293/hTLR4a cells.

Preparation of Recombinant hMD-2 in Pichia pastoris and Purification. hMD-2 was produced in *Pichia pastoris*, analyzed by SDS−PAGE, and its biological activity tested on 293/hTLR4a cells.

The coding sequence of mature hMD-2 was amplified by PCR (primers F-hMD2-Q19 CAGAAGCAGTATTGGGTCTGC and R-Spe-hMD2 TTTACTAGTATTTGAATTAGGTTGGTGTAGG) from a plasmid template and ligated into the SnaBI/SpeI opened pPpT4AlphaS-His expression vector (under the control of AOX1 promoter), in frame with the N-terminal *S. cerevisiae* α-MF prepro leader sequence and the C-terminal 6xHis tag. The resulting recombinant plasmid pPpT4AlphaS-His was transformed into *E. coli* DH5α competent cells, and the positive recombinant plasmid, which was confirmed by DNA sequencing, was linearized and transformed into *Pichia pastoris* GS115 by electroporation. MD-2 expressing transformant was selected and cultured in a 250 mL shake flask containing 10 mL of YPD liquid media at 28 °C for 24 h. Two liter flasks containing 250 mL of BMGY (1% glycerol) medium at 28 °C were inoculated with 1 mL of overnight inoculum. After being cultured for 24 h, cells were aseptically collected by centrifugation at room temperature for 10 min at 5000 rpm. BMGY medium was replaced with 250 mL of methanol-complex medium BMMY (1% methanol) to induce protein expression at 28 °C (250 rpm), adding 1% of methanol every 12 h. After 2 days of fermentation in BMMY, cells were removed by centrifugation 10 min at 5000 rpm. Supernatant was supplemented with 2 mM $MgCl_2$ (Sigma) and d100 mg/L of reduced glutathione (Sigma), and pH was adjusted to 7.5 with NaOH (Sigma). Precipitate was removed by centrifugation for 20 min at 1900*g*, followed by filtration using Stericup-GP 0.22 μm (Sigma). A 0.5 M solution of Tris HCl pH 7.5 and 1.5 M NaCl (Sigma) was added to the medium to a final concentration of 50 mM Tris HCl and 150 mM NaCl. High density nickel resin (ABT) was added to the medium (30 mL every liter of medium) and incubated in batch at room temperature for 4 h. High density nickel resin was washed several times with 50 mM Tris HCl pH 7.5 and 150 mM NaCl solution. hMD-2 was eluted with 0.5 M imidazole (Sigma) in 2 mL fractions, which were analyzed for protein concentration and by SDS-PAGE. Pooled fractions containing hMD-2 were extensively dialyzed against 50 mM Tris, 150 mM NaCl, and 0.5% Tween 20, pH 7.5 at 4 °C, and purified hMD-2 biological activity was tested on 293/hTLR4a cells.

Preparation of Recombinant hMD-2 in Mammalian Cells and Purification. hMD-2 was produced in HEK293T cells, analyzed by SDS−PAGE, and its biological activity tested on 293/hTLR4a cells.

HEK293T cells were grown in high-glucose DMEM medium supplemented with 10% fetal calf serum, 106 units per L of penicillin G and 1 g L−L of streptomycin in a 5% CO_2 atmosphere at 37 °C. Mammalian expression constructs for secreted proteins carrying a N-terminal FLAG-tag were generated in the pEF vector (Thermo Fisher Scientific). pEF-Flag-DEVD-hMD2-myc/His plasmid was transiently transfected to HEK293T cells, and the cells were harvested 48 h after transfection and resuspended in lysis buffer containing 50 mM Tris, 150 mM NaCl, 1 mM EDTA, and 1% TRITON X-100. The cell suspension was homogenized by Dounce homogenizer and clarified by centrifugation at 10,000*g* for 20 min. ANTI-FLAG M2 affinity gel beads (SIGMA) was added to the lysate, and then it was left shaking at 4 °C overnight. Solution was spin down at 1000 rpm for 2 min and eluted with TBS Flag peptide (100 μL/mL). Recombinant protein hMD-2 was confirmed by Western blot analysis using an HRP-coupled antibody directed against the FLAG-tag at 1:5000 dilution ratio (Invitrogen).

SDS-PAGE and Western Blot. Purified recombinant hMD-2 was analyzed on 15% SDS-PAGE under reducing conditions followed by Coomassie Brilliant Blue staining. For Western blot analysis, proteins were separated by SDS-PAGE under reducing conditions and then electrophoretically transferred onto polyvinylidene difluoride mem-

DOI: 10.1021/acs.jmedchem.7b01803
J. Med. Chem. 2018, 61, 2895−2909

branes (Amersham Biosciences). After protein transfer, the membranes were treated with blocking buffer followed by incubation with anti-His-HRP antibodies (Sigma). Then, the bands were visualized by 3,3′-diaminobenzidine (Sigma) as a peroxidase substrate.

Protein Concentration Determination. The total protein concentration was determined using ultraviolet absorption at 280 nm. The theoretical extinction coefficient (19.285) was obtained using the protein sequence of hMD-2.

hMD-2 Activity Test Using 293/hTLR4a Cells. For measuring the activity of recombinant expressed hMD-2, HEK 293 cells stably transfected with the human TLR4a gene (293/hTLR4a (Invivogen)) were used. Various dilutions of hMD-2 (stock concentration was 10 μM) were incubated with 100 ng/mL of LPS (Sigma) prior to stimulation of 293/hTLR4a cells. Supernatants were analyzed for IL-8 secretion by ELISA assay.

Determination of IL-8 Secretion by Sandwich Enzyme-Linked Immunosorbent Assay. IL-8 concentrations were assayed using the IL-8 Cytosets (Invitrogen) antibody pair kit containing matched, pretitrated, and fully optimized capture and detection antibodies, recombinant IL-8 standard, and streptavidin-horseradish peroxidase (Sigma). The assay was conducted according to the manufacturer's specifications.

Antibody-Sandwich ELISA for the Detection of Binding of Compounds to hMD-2. The method of antibody-sandwich ELISA for the detection of the binding of compounds to MD-2 was modified from a previous study.[36] A microtiter plate was coated overnight at 4 °C with 100 μL/well of 5 μg/mL of chicken polyclonal anti-hMD-2 antibodies, diluted in 50 mM Na_2CO_3 buffer, pH 9.6, and blocked with 1% BSA in PBS. After washing, 1 μM hMD-2 with tested compounds was added and incubated for 2 h. Mouse anti-hMD-2 mAb (0.1 μg/mL, 9B4) and goat antimouse IgG conjugated with HRP (0.1 μg/mL) in PBS were added, followed by detection at 420 nm after the addition of 100 μL of ABTS (Sigma). Chicken anti-hMD-2 polyclonal antibodies were prepared against recombinant hMD-2 by GenTel (Madison, WI, USA), monoclonal mouse anti-hMD-2 9B4 antibodies were from eBioscience (San Diego, CA, USA), and secondary goat antimouse IgG conjugated with horseradish peroxidase was from Santa Cruz Biotechnology (Santa Cruz, CA, USA).

Fluorescence Spectroscopy Assay. Fluorescence was measured on PerkinElmer fluorimeter LS 55 (PerkinElmer, UK) as previously described.[38] All measurements were done at 20 °C in a 5 × 5 mm quartz glass cuvette (Hellma Suprasil, Müllheim, Germany). hMD-2 protein (200 nM) and 1,1′-Bis(anilino)-4,4′-bis (naphthalene)-8,8′ disulfonate (bis-ANS, 200 nM) were mixed and incubated until reaching stable relative fluorescence units (RFUs) emitted at 420−550 nm under excitation at 385 nm. Compounds, at different concentrations, were then added, followed by relative fluorescence unit (RFU) measurement at 420−550 nm.

LPS Displacement Assay. The ability of the compounds to displace LPS from hMD-2 hydrophobic pocket was determined by ELISA. A microtiter plate was coated overnight at 4 °C with 100 μL/well of 5 μg/mL chicken polyclonal anti-hMD-2 antibodies, diluted in 50 mM Na_2CO_3 buffer, pH 9.6, and blocked with 1% BSA in PBS. After washing, 1 μM hMD-2 with biotin-labeled LPS was added and incubated for 2 h. After washing, the compounds were added at different concentrations and incubated for 1.5 h. After washing, 0.5 μg/mL HRP-conjugated streptavidin (Sigma) in PBS was added, followed by detection at 420 nm after the addition of 100 μL of ABTS (Sigma). Chicken anti-hMD-2 polyclonal antibodies were prepared against recombinant hMD-2 by GenTel (Madison, WI, USA).

Surface Plasmon Resonance (SPR) Analysis. The binding affinity of the compounds to recombinant hMD-2 was determined using a Biacore X100 with an NTA sensor chip (Biacore, GE Healthcare, Uppsala, Sweden). Briefly, 0.5 μM hMD-2 (in 50 mM Tris, 150 mM NaCl, 0.5% Tween 20, pH 7.5) was immobilized onto the sensor chip previously activated with 1 min pulse of 10 mM $NiSO_4$. The first flow cell was used as a reference surface to control nonspecific binding. Both flow cells were injected with the analyte (in PBS, 5% DMSO, 5% EtOH, pH 7.5) at a flow rate of 10 μL/min at 25 °C in increasing concentrations. The data were analyzed with Biacore Evaluation software. K_D values were calculated by global fitting of the equilibrium binding responses from various concentrations of analytes using a 1:1 Langmuir binding model.

■ ASSOCIATED CONTENT

Supporting Information

. The Supporting Information is available free of charge on the ACS Publications website at DOI: 10.1021/acs.jmedchem.7b01803.

Molecular formula strings (CSV)

Molecular modeling; docking results; FT-IR spectroscopy; NMR spectroscopy; small-angle X-ray scattering; synthesis and compounds characterization (PDF)

■ AUTHOR INFORMATION

Corresponding Author

*E-mail: francesco.peri@unimib.it. Phone: +39.0264483453.

ORCID

Fabio A. Facchini: 0000-0002-4339-5845
Cristina Airoldi: 0000-0002-3670-6262
Roman Jerala: 0000-0002-6337-5251
Francesco Peri: 0000-0002-3417-8224

Notes

The authors declare no competing financial interest.

■ ACKNOWLEDGMENTS

This study was financially supported by the H2020-MSC-ETN-642157 project TOLLerant. The Italian Ministry for Foreign Affairs and International Cooperation (MAECI), the Slovenian National Agency (grant P4-0176) and the Spanish Ministry for Economy and Competitiveness (MINECO, grants CTQ2014-57141-R and CTQ2017-88353-R) are also acknowledged. SAXS measurements were performed at the EMBL beamline P12 c/o DESY, Hamburg, Germany (beam time grant to A.B.S).

■ ABBREVIATIONS USED

TLR, Toll-like receptor; PRRs, pattern recognition receptors; PAMPs, pathogen-associated molecular patterns; MD-2, myeloid differentiation 2; LOS, lipooligosaccharide; DAMPs, damage-associated molecular patterns; LBP, lipid binding protein; CD14, cluster of differentiation 14

■ REFERENCES

(1) Akira, S.; Takeda, K. Toll-like receptor signalling. *Nat. Rev. Immunol.* **2004**, *4*, 499−511.

(2) Molinaro, A.; Holst, O.; Di Lorenzo, F.; Callaghan, M.; Nurisso, A.; D'Errico, G.; Zamyatina, A.; Peri, F.; Berisio, R.; Jerala, R.; Jiménez-Barbero, J.; Silipo, A.; Martín-Santamaría, S. Chemistry of lipid A: at the heart of innate immunity. *Chem. - Eur. J.* **2015**, *21*, 500−519.

(3) Krüger, C. L.; Zeuner, M. T.; Cottrell, G. S.; Widera, D.; Heilemann, M. Quantitative single-molecule imaging of TLR4 reveals ligand-specific receptor dimerization. *Sci. Signaling* **2017**, *10*, eaan1308.

(4) Gioannini, T.; Teghanemt, A.; Zhang, D.; Levis, E.; Weiss, J. Monomeric endotoxin: protein complexes are essential for TLR4-dependent cell activation. *J. Endotoxin Res.* **2005**, *11*, 117−123.

(5) Park, B.; Song, D.; Kim, H.; Choi, B.; Lee, H.; Lee, J. The structural basis of lipopolysaccharide recognition by the TLR4-MD-2 complex. *Nature* **2009**, *458*, 1191−1195.

(6) Cighetti, R.; Ciaramelli, C.; Sestito, S. E.; Zanoni, I.; Kubik, Ł.; Ardá-Freire, A.; Calabrese, V.; Granucci, F.; Jerala, R.; Martín-Santamaría, S.; Jiménez-Barbero, J.; Peri, F. Modulation of CD14

DOI: 10.1021/acs.jmedchem.7b01803
J. Med. Chem. 2018, 61, 2895−2909

and TLR4·MD-2 activities by a synthetic lipid A mimetic. *ChemBioChem* **2014**, *15*, 250−258.
(7) Okamura, Y.; Watari, M.; Jerud, E.; Young, D.; Ishizaka, S.; Rose, J.; Chow, J.; Strauss, J. r. The extra domain A of fibronectin activates toll-like receptor 4. *J. Biol. Chem.* **2001**, *276*, 10229−10233.
(8) Wang, Y.; Qian, Y.; Fang, Q.; Zhong, P.; Li, W.; Wang, L.; Fu, W.; Zhang, Y.; Xu, Z.; Li, X.; Liang, G. Saturated palmitic acid induces myocardial inflammatory injuries through direct binding to TLR4 accessory protein MD-2. *Nat. Commun.* **2017**, *8*, 13997.
(9) Mancek-Keber, M.; Frank-Bertoncelj, M.; Hafner-Bratkovič, I.; Smole, A.; Zorko, M.; Pirher, N.; Hayer, S.; Kralj-Iglic, V.; Rozman, B.; Ilc, N.; Horvat, S.; Jerala, R. Toll-like receptor 4 senses oxidative stress mediated by the oxidation of phospholipids in extracellular vesicles. *Sci. Signaling* **2015**, *8*, ra60.
(10) Goligorsky, M. S. TLR4 and HMGB1: partners in crime? *Kidney Int.* **2011**, *80*, 450−452.
(11) Erridge, C. The roles of toll-like receptors in atherosclerosis. *J. Innate Immun.* **2009**, *1*, 340−349.
(12) Abdollahi-Roodsaz, S.; Joosten, L. A.; Roelofs, M. F.; Radstake, T. R.; Matera, G.; Popa, C.; van der Meer, J. W.; Netea, M. G.; van den Berg, W. B. Inhibition of toll-like receptor 4 breaks the inflammatory loop in autoimmune destructive arthritis. *Arthritis Rheum.* **2007**, *56*, 2957−2967.
(13) Cao, L.; Tanga, F.; Deleo, J. The contributing role of CD14 in toll-like receptor 4 dependent neuropathic pain. *Neuroscience* **2009**, *158*, 896−903.
(14) Casula, M.; Iyer, A. M.; Spliet, W. G.; Anink, J. J.; Steentjes, K.; Sta, M.; Troost, D.; Aronica, E. Toll-like receptor signaling in amyotrophic lateral sclerosis spinal cord tissue. *Neuroscience* **2011**, *179*, 233−43.
(15) Fan, J.; Li, Y.; Levy, R. M.; Fan, J. J.; Hackam, D. J.; Vodovotz, Y.; Yang, H.; Tracey, K. J.; Billiar, T. R.; Wilson, M. A. Hemorrhagic shock induces NAD(P)H oxidase activation in neutrophils: role of HMGB1-TLR4 signaling. *J. Immunol.* **2007**, *178*, 6573−6580.
(16) Kuzmich, N. N.; Sivak, K. V.; Chubarev, V. N.; Porozov, Y. B.; Savateeva-Lyubimova, T. N.; Peri, F. TLR4 Signaling pathway modulators as potential therapeutics in inflammation and sepsis. *Vaccines (Basel, Switz.)* **2017**, *5*, 34.
(17) Opal, S. M.; Laterre, P. F.; Francois, B.; LaRosa, S. P.; Angus, D. C.; Mira, J. P.; Wittebole, X.; Dugernier, T.; Perrotin, D.; Tidswell, M.; Jauregui, L.; Krell, K.; Pachl, J.; Takahashi, T.; Peckelsen, C.; Cordasco, E.; Chang, C. S.; Oeyen, S.; Aikawa, N.; Maruyama, T.; Schein, R.; Kalil, A. C.; Van Nuffelen, M.; Lynn, M.; Rossignol, D. P.; Gogate, J.; Roberts, M. B.; Wheeler, J. L.; Vincent, J. L. Effect of eritoran, an antagonist of MD-2/TLR4, on mortality in patients with severe sepsis: the ACCESS randomized trial. *JAMA* **2013**, *309*, 1154−1162.
(18) Rice, T.; Wheeler, A.; Bernard, G.; Vincent, J.; Angus, D.; Aikawa, N.; Demeyer, I.; Sainati, S.; Amlot, N.; Cao, C.; Ii, M.; Matsuda, H.; Mouri, K.; Cohen, J. A randomized, double-blind, placebo-controlled trial of TAK-242 for the treatment of severe sepsis. *Crit. Care Med.* **2010**, *38* (8), 1685−1694.
(19) Salluh, J. I.; Póvoa, P. Biomarkers as end points in clinical trials of severe sepsis: a garden of forking paths. *Crit. Care Med.* **2010**, *38*, 1749−1751.
(20) Kalil, A. C.; LaRosa, S. P.; Gogate, J.; Lynn, M.; Opal, S. M. Influence of severity of illness on the effects of eritoran tetrasodium (E5564) and on other therapies for severe sepsis. *Shock* **2011**, *36*, 327−331.
(21) Danner, R. L.; Van Dervort, A. L.; Doerfler, M. E.; Stuetz, P.; Parrillo, J. E. Antiendotoxin activity of lipid A analogues: requirements of the chemical structure. *Pharm. Res.* **1990**, *7*, 260−263.
(22) Matsuura, M.; Kiso, M.; Hasegawa, A. Activity of monosaccharide lipid A analogues in human monocytic cells as agonists or antagonists of bacterial lipopolysaccharide. *Infect. Immun.* **1999**, *67*, 6286−6292.
(23) Yang, D.; Satoh, M.; Ueda, H.; Tsukagoshi, S.; Yamazaki, M. Activation of tumor-infiltrating macrophages by a synthetic lipid A analog (ONO-4007) and its implication in antitumor effects. *Cancer Immunol. Immunother.* **1994**, *38*, 287−293.
(24) Tamai, R.; Asai, Y.; Hashimoto, M.; Fukase, K.; Kusumoto, S.; Ishida, H.; Kiso, M.; Ogawa, T. Cell activation by monosaccharide lipid A analogues utilizing toll-like receptor 4. *Immunology* **2003**, *110*, 66−72.
(25) Perrin-Cocon, L.; Aublin-Gex, A.; Sestito, S. E.; Shirey, K. A.; Patel, M. C.; Andre, P.; Blanco, J. C.; Vogel, S. N.; Peri, F.; Lotteau, V. TLR4 antagonist FP7 inhibits LPS-induced cytokine production and glycolytic reprogramming in dendritic cells, and protects mice from lethal influenza infection. *Sci. Rep.* **2017**, *7*, 40791.
(26) Funatogawa, K.; Matsuura, M.; Nakano, M.; Kiso, M.; Hasegawa, A. Relationship of structure and biological activity of monosaccharide lipid A analogues to induction of nitric oxide production by murine macrophage RAW264.7 cells. *Infect. Immun.* **1998**, *66*, 5792−5798.
(27) Mueller, M.; Lindner, B.; Kusumoto, S.; Fukase, K.; Schromm, A. B.; Seydel, U. Aggregates are the biologically active units of endotoxin. *J. Biol. Chem.* **2004**, *279*, 26307−26313.
(28) Gutsmann, T.; Schromm, A.; Brandenburg, K. The physicochemistry of endotoxins in relation to bioactivity. *Int. J. Med. Microbiol.* **2007**, *297*, 341−352.
(29) Gioannini, T.; Teghanemt, A.; Zhang, D.; Coussens, N.; Dockstader, W.; Ramaswamy, S.; Weiss, J. Isolation of an endotoxin-MD-2 complex that produces toll-like receptor 4-dependent cell activation at picomolar concentrations. *Proc. Natl. Acad. Sci. U. S. A.* **2004**, *101*, 4186−4191.
(30) Ciaramelli, C.; Calabrese, V.; Sestito, S. E.; Pérez-Regidor, L.; Klett, J.; Oblak, A.; Jerala, R.; Piazza, M.; Martín-Santamaría, S.; Peri, F. Glycolipid-based TLR4 modulators and fluorescent probes: rational design, synthesis, and biological properties. *Chem. Biol. Drug Des.* **2016**, *88*, 217−229.
(31) Liu, M.; Nicholson, J. K.; Lindon, J. C. High-resolution diffusion and relaxation edited one- and two-dimensional ^{1}H NMR spectroscopy of biological fluids. *Anal. Chem.* **1996**, *68*, 3370−3376.
(32) Beckonert, O.; Keun, H. C.; Ebbels, T. M. D.; Bundy, J.; Holmes, E.; Lindon, J. C.; Nicholson, J. K. Metabolic profiling, metabolomic and metabonomic procedures for NMR spectroscopy of urine, plasma, serum and tissue extracts. *Nat. Protoc.* **2007**, *2*, 2692.
(33) Manček-Keber, M.; Jerala, R. Postulates for validating TLR4 agonists. *Eur. J. Immunol.* **2015**, *45*, 356−370.
(34) Ohnishi, T.; Muroi, M.; Tanamoto, K.-i. N-Linked Glycosylations at Asn26 and Asn114 of Human MD-2 Are Required for toll-like receptor 4-mediated activation of NF-kB by lipopolysaccharide. *J. Immunol.* **2001**, *167*, 3354−3359.
(35) da Silva Correia, J.; Ulevitch, R. J. MD-2 and TLR4 N-linked glycosylations are important for a functional lipopolysaccharide receptor. *J. Biol. Chem.* **2002**, *277*, 1845−1854.
(36) Viriyakosol, S.; McCray, P. B.; Ashbaugh, M. E.; Chu, J.; Jia, H. P.; Weiss, J.; Kirkland, T. N. Characterization of monoclonal antibodies to human soluble MD-2 protein. *Hybridoma* **2006**, *25*, 349−357.
(37) Resman, N.; Gradisar, H.; Vasl, J.; Keber, M.; Pristovsek, P.; Jerala, R. Taxanes inhibit human TLR4 signaling by binding to MD-2. *FEBS Lett.* **2008**, *582*, 3929−3934.
(38) Mancek-Keber, M.; Jerala, R. Structural similarity between the hydrophobic fluorescent probe and lipid A as a ligand of MD-2. *FASEB J.* **2006**, *20*, 1836−1842.
(39) Ohto, U.; Fukase, K.; Miyake, K.; Shimizu, T. Structural basis of species-specific endotoxin sensing by innate immune receptor TLR4/MD-2. *Proc. Natl. Acad. Sci. U. S. A.* **2012**, *109*, 7421−7426.
(40) Brandenburg, K.; Matsuura, M.; Heine, H.; Müller, M.; Kiso, M.; Ishida, H.; Koch, M. H. J.; Seydel, U. Biophysical characterization of triacyl monosaccharide lipid a partial structures in relation to bioactivity. *Biophys. J.* **2002**, *83*, 322−333.
(41) Seydel, U.; Schromm, A. B.; Brade, L.; Gronow, S.; Andrä, J.; Müller, M.; Koch, M. H. J.; Fukase, K.; Kataoka, M.; Hashimoto, M.; Kusumoto, S.; Brandenburg, K. Physicochemical characterization of

DOI: 10.1021/acs.jmedchem.7b01803
J. Med. Chem. 2018, 61, 2895−2909

carboxymethyl lipid A derivatives in relation to biological activity. *FEBS J.* **2005**, *272*, 327−340.

(42) *The PyMOL Molecular Graphics System*, version 1.8; Schrodinger, LLC, 2015.

(43) Sestito, S. E.; Facchini, F. A.; Morbioli, I.; Billod, J.-M.; Martin-Santamaria, S.; Casnati, A.; Sansone, F.; Peri, F. Amphiphilic guanidinocalixarenes inhibit lipopolysaccharide (LPS)- and lectin-stimulated toll-like receptor 4 (TLR4) Signaling. *J. Med. Chem.* **2017**, *60*, 4882−4892.

(44) Case, D. A.; Babin, V.; Berryman, J.; Betz, R.; Cai, Q.; Cerutti, D.; Cheatham, T.; Darden, T.; Duke, R.; Gohlke, H.; Götz, A.; Gusarov, S.; Homeyer, N.; Janowski, P.; Kaus, J.; Kolossváry, I.; Kovalenko, A.; Lee, T.-S.; Legrand, S.; A. Kollman, P. *Amber 2014*; University of California, San Francisco, 2014.

(45) Frisch, M. J.; Schlegel, H. B.; Scuseria, G. E.; Robb, M. A.; Cheeseman, J. R.; Scalmani, G.; Barone, V.; Mennucci, B.; Petersson, G. A.; Nakatsuji, H.; Caricato, M.; Li, X.; Hratchian, H. P.; Izmaylov, A. F.; Bloino, J.; Zheng, G.; Sonnenberg, J. L.; Hada, M.; Ehara, M.; Toyota, K.; Fukuda, R.; Hasegawa, J.; Ishida, M.; Nakajima, T.; Honda, Y.; Kitao, O.; Nakai, H.; Vreven, T.; Montgomery, J. A., Jr.; Peralta, J. E.; Ogliaro, F.; Bearpark, M. J.; Heyd, J.; Brothers, E. N.; Kudin, K. N.; Staroverov, V. N.; Kobayashi, R.; Normand, J.; Raghavachari, K.; Rendell, A. P.; Burant, J. C.; Iyengar, S. S.; Tomasi, J.; Cossi, M.; Rega, N.; Millam, N. J.; Klene, M.; Knox, J. E.; Cross, J. B.; Bakken, V.; Adamo, C.; Jaramillo, J.; Gomperts, R.; Stratmann, R. E.; Yazyev, O.; Austin, A. J.; Cammi, R.; Pomelli, C.; Ochterski, J. W.; Martin, R. L.; Morokuma, K.; Zakrzewski, V. G.; Voth, G. A.; Salvador, P.; Dannenberg, J. J.; Dapprich, S.; Daniels, A. D.; Farkas, Ö.; Foresman, J. B.; Ortiz, J. V.; Cioslowski, J.; Fox, D. J. *Gaussian 09*; Gaussian, Inc.: Wallingford, CT, 2009.

(46) Kirschner, K. N.; Yongye, A. B.; Tschampel, S. M.; GonzÁLez-OuteiriÑO, J.; Daniels, C. R.; Foley, B. L.; Woods, R. J. GLYCAM06: a generalizable biomolecular force field. Carbohydrates. *J. Comput. Chem.* **2008**, *29*, 622−655.

(47) Morris, G. M.; Huey, R.; Lindstrom, W.; Sanner, M. F.; Belew, R. K.; Goodsell, D. S.; Olson, A. J. Autodock4 and Autodocktools4: automated docking with selective receptor flexibility. *J. Comput. Chem.* **2009**, *30*, 2785−2791.

(48) *Maestro*, release 2017−4; Schrödinger, LLC: New York, 2017.

(49) Gruber, A.; Mancek, M.; Wagner, H.; Kirschning, C. J.; Jerala, R. Structural model of MD-2 and functional role of its basic amino acid clusters involved in cellular lipopolysaccharide recognition. *J. Biol. Chem.* **2004**, *279*, 28475−28482.

DOI: 10.1021/acs.jmedchem.7b01803
J. Med. Chem. 2018, 61, 2895−2909